

Master's thesis

NTNU
Norwegian University of Science and Technology
Faculty of Information Technology and Electrical
Engineering
Department of Mathematical Sciences

Thibault Edward Gaudet

Upscaling models of CO₂ migration through low-permeable layers in porous media

Master's thesis in MSMNFMA

Supervisor: Knut-Andreas Lie, Halvor Nilsen

June 2020



Norwegian University of
Science and Technology

Thibault Edward Gaudet

Upscaling models of CO₂ migration through low-permeable layers in porous media

Master's thesis in MSMNFMA
Supervisor: Knut-Andreas Lie, Halvor Nilsen
June 2020

Norwegian University of Science and Technology
Faculty of Information Technology and Electrical Engineering
Department of Mathematical Sciences



Norwegian University of
Science and Technology

Summary

In this thesis we investigate methods preserving the effects of thin layers of rock with low permeability on flow behaviour while upscaling geological models of porous media. More specifically, we study this upscaling in the context of upward migration of CO₂ in the process of Carbon Capture and Storage (CCS).

Three methods are implemented and investigated. The first method consists of harmonic averaging the permeability onto coarser grids. This is proven to be an insufficient choice for upscaling. The second and third methods rely on computing appropriate permeability and transmissibility fields respectively on coarse grids based on the reservoir and rock's geophysical parameters. An analysis of the fields' dependence on these parameters is conducted for each method. This analysis concludes that both methods, although generating a flow similar to the flow observed on a fine grid in specific cases, can potentially lead to errors in flow behaviour modelling and must thus be used with caution.

Preface

This thesis has been written as part of the Master's degree programme in Mathematical Sciences with specialisation in Applied Mathematics at the Norwegian University of Science and Technology (NTNU) and was conducted in cooperation with SINTEF Digital, Mathematics and Cybernetics department located in Oslo.

I would like to express my gratitude to my supervisor, Knut-Andreas Lie, for his guidance and patience during the whole writing process of this thesis. I would also like to thank my co-supervisor, Halvor Nilsen, and the whole team at SINTEF with whom I had very interesting discussions when I visited them during the first semester.

I also want to say how grateful I am to Lola Rousseau, my ever-supporting partner, for being there for me and for continuously encouraging me to give my best especially during this tough year.

Finally, I would like to thank my parents, my sister, and friends for their unwavering support. Knowing I could count on when needed means a lot to me.

Table of Contents

Summary	i
Preface	ii
Table of Contents	iv
1 Introduction	1
1.1 Outline of the thesis	3
2 Background Theory	5
2.1 Underground reservoir's geological properties	5
2.1.1 Porosity	5
2.1.2 Permeability	6
2.1.3 Representative Elementary Volume (REV)	6
2.2 Single-phase flow	7
2.2.1 Darcy's law	7
2.2.2 Single-phase problem formulation	8
2.3 Multiphase flow	8
2.3.1 Wettability	9
2.3.2 Capillary pressure	10
2.3.3 Relative permeabilities	11
2.3.4 The fractional flow model	12
2.4 Analytical solutions for 1D flow	14
2.4.1 A first approach in horizontal homogeneous media	14
2.4.2 Flow in vertical homogeneous media	20
2.4.3 Flow in inhomogeneous vertical media	23
3 MRST and model set-up	27
3.1 MATLAB Reservoir Simulation Toolbox (MRST)	27
3.1.1 The Two-Point Flux Approximation (TPFA)	27
3.2 Medium definition and fine grid model	28

4 Experiments	35
4.1 Harmonic average of the permeability field	35
4.1.1 Experiment description	35
4.1.2 Results	36
4.1.3 Overview and discussion	40
4.2 Functional relationship for the permeability field	42
4.2.1 Experiment description	42
4.2.2 Results	42
4.2.3 Overview and discussion	51
4.3 Changes in the transmissibility	53
4.3.1 Experiment description	53
4.3.2 Results	54
4.3.3 Overview and discussion	59
5 Conclusion	63
5.1 Summary and conclusion	63
5.2 Further work	64
Bibliography	65

Chapter 1

Introduction

Approximately a hundred million barrels of oil are produced and consumed every day worldwide, and current predictions estimate that this number will continue to grow in the coming years, despite a significant drop due to the COVID-19 pandemic (U.S. Energy Information Administration, 2020). However, the general awareness about human activities' impact on the planet has increased and the scientific community who stressed the importance of reducing the emissions of greenhouse gas for decades is receiving more support from the public and the decision makers.

Anthropogenic climate change intensity and its impacts can be mitigated through the combination of three approaches (Keith and Dowlatabadi, 1992): either humans redefine their activities to limit their contribution to global warming, or they can "accept" climate change and look for innovations that will help overcome its effects, and finally develop technologies to intervene at the climate scale and reduce the amplitude of the climate change. The latter approach regroups technologies called geoengineering options which are concepts or technologies that aim to decrease the impact of climate change without imposing drastic repercussions on human behaviour. Among these geoengineering options, Carbon Capture and Storage (CCS) has grown popular in the last decade. In its latest report, the International Panel on Climate Change (IPCC) heavily relies on the use of CCS to reduce the net emissions of carbon dioxide (CO_2) (IPCC, 2018). CCS consists of three steps: capture of CO_2 , transportation and finally storage of CO_2 (Energy Institute (Great Britain), 2010).

There currently exist two ways to store CO_2 : either under a solid (or mineral) form or under a gaseous form. Storage of gaseous/supercritical CO_2 is done by injecting it into a variety of underground geological formations. Examples of such formations are aquifers, and old oil and gas production fields that have been depleted. These underground formations, also referred to as reservoirs, can be described as porous media which means that they have a capacity to store fluids. Studying the flow behaviour of carbon dioxide in such reservoirs must be done through modelling, since it is not possible to observe the flows directly. Fortunately, petroleum extraction has had to deal with the same constraints

and hence developed tools and methodologies, including reservoir engineering, to analyse and anticipate the flow behaviour of chemical species trapped in underground reservoirs. Ironically, modelling flow of CO₂ for CCS relies on the same tools developed by the very same industry that led to the necessity of implementing geoengineering options such as CCS. A good knowledge of the reservoir's geophysical structure is essential to perform high quality numerical simulations to determine the quantity of carbon dioxide a burial site can receive and how it will behave once injected in the receptacle.

Evaluating the geophysical parameters of reservoirs can be done either by direct measurements from rock samples or indirectly, through seismic data for instance. Although these methods must cope with a certain degree of uncertainty either in the measurements or when computing the values of the parameters elsewhere in the reservoir based on these measurements, it is conceivable that the structure and physical parameters of the reservoir are determined with a good resolution. This in turn leads to very precise and accurate flow behaviour estimates. However, most underground formations typically spread over several kilometers on the horizontal axis and up to a few hundred meters vertically, which means that modelling them precisely over their whole volume requires storage of a lot of information (often up to 10⁶-10⁷ cells). Additionally, having a detailed model increases the run-time for simulations. One alternative to bypass these issues is to consider modelling reservoirs with less precision but doing so might introduce errors in the predictions of flow behaviour. In an attempt to mitigate these undesired induced errors, reservoir engineers use a process called model reduction, or upscaling, that aims to diminish the resolution of the grids representing underground reservoirs while preserving the key flow behaviour's characteristics. Upscaling requires among other things to determine new values of physical variables on coarser grids, often computed using some form of average of the values from the finer grid.

Although in-depth geology is out of the scope of this thesis, it is interesting to describe the formation of a typical underground reservoir. It consists of an accumulation of layers of sediment, usually formed near water streams that carry these sediments (Lie, 2019). As time passes, these layers thicken and the future reservoir grows in size. It is important to note that different climate and geographical conditions create different types of sedimentary rocks. Hence, it is not unusual to find large differences in the rock composition on the scale of a few centimeters. In particular, when conditions are met, thin impermeable or low-permeable layers can form in between two large layers with higher permeability. Once the reservoir sinks underground under its own weight, these thin layers might not be thicker than half a meter which is substantially smaller than the scale on which reservoirs typically spread. Still, these impermeable layers will act as barriers that slow or block flows of entities trapped in the reservoir (e.g., water, oil, or gas) despite their relatively low thickness. Therefore, one must be careful when attempting to upscale the reservoir modelling grid on the vertical axis as these small-sized objects have large impacts on the global flow behaviour that cannot be disregarded.

Upscaling low-permeable layers when decreasing the vertical resolution is not limited to CCS. In a somewhat related field, the injection or storage of dihydrogen H₂ in reservoir for future use as an energy source would essentially face similar challenges that the storage of CO₂ does, and upscaling these low-permeable layers is one of them. Another example

in porous media where this upscaling process would be crucial is the study of pollutant infiltration in the ground which may cause ground-water contamination.

The aim of this thesis is to point out and investigate potential upscaling methods for the vertical migration of CO₂ in the context of simplified reservoirs with horizontal low-permeable layers. The main goal is to assess the performance of each method, inspect and discuss their eventual limits, and determine whether they can be deemed trustworthy to accurately model the effects of thin low-permeable layers for a broader spectrum of reservoirs.

1.1 Outline of the thesis

In Chapter 2 we start by introducing the key concepts in reservoir modelling, from the definition of the geophysical parameters to the derivation of the equations governing the system. Chapter 3 details the specific reservoir model on which simulations will be performed and gives a first overview of the behaviour that the implemented methods will be expected to reproduce. Chapter 4 consists of experiments on the upscaling methods aiming to model the effects of a low-permeability layer. Each method is described, tested, analysed, and discussed. A summary of the work is provided in Chapter 5 and we also lay the ground for future work after discussing potential research directions.

Chapter 2

Background Theory

2.1 Underground reservoir's geological properties

2.1.1 Porosity

Porosity is an indicator of the rock's voidness and is determined as the ratio between the volume of pores over the overall volume. It will be denoted ϕ .

By definition, porosity is always positive and can never reach (nor exceed) 1. Thus, we have $0 \leq \phi < 1$. Porosity is used to establish the ability of a rock to store fluids: the lower the porosity, the less void space there is in the rock which prevents fluid to be stored in great quantities and vice-versa.

For accuracy purposes, one can also define the effective porosity ϕ_{eff} to take into account that some of the pore space is actually disconnected and hence does not play any role in the global fluid movements. This can be translated into $0 \leq \phi_{\text{eff}} \leq \phi < 1$. This also means that the parameter of interest when studying the potential storage volume and the flow behaviour is the effective porosity ϕ_{eff} . However, for notation simplifications, the effective porosity will be referred to as ϕ . Porosity values are generally within the range of 0.05-0.5 (Eiken et al., 2011; Lie, 2019).

While porosity in rigid media is considered to be static, porosity in non-rigid medium is commonly modelled as dependant of the pressure. One way to handle this dependence is to define the rock's compressibility by

$$c_r = \frac{1}{\phi} \frac{d\phi}{dp} = \frac{d \ln(\phi)}{dp}, \quad (2.1)$$

where p is the overall reservoir pressure.

2.1.2 Permeability

While porosity describes the rock's storing capacity, permeability is the parameter which quantifies how a fluid flows through the rock and how it is transmitted from pores to pores. Permeability is denoted by $K [m^2]$ and is usually given by a full tensor

$$K = \begin{bmatrix} K_{xx} & K_{xy} & K_{xz} \\ K_{yx} & K_{yy} & K_{yz} \\ K_{zx} & K_{zy} & K_{zz} \end{bmatrix}. \quad (2.2)$$

The diagonal coefficients K_{xx} , K_{yy} and K_{zz} from the tensor (2.2) illustrate the impact a pressure drop in one axial direction has on the flow rate for this same direction. The same goes for off-diagonal elements which describe how the flow rate along a direction is affected by pressure drops in perpendicular directions.

In an isotropic medium, this tensor can be reduced to a simple scalar. Although the anisotropic case does not benefit from this level of simplification, one can still get that this tensor is both symmetric and positive definite (Lie, 2019).

Values of permeability are often given in unit "darcy" (d) with $1 \text{ d} \simeq 0.987 \times 10^{-12} \text{ m}^2$ as it is overall better suited for permeability values usually encountered in oil reservoirs or aquifers. These values can vary a lot from reservoir to reservoir but also within a reservoir itself as described in the introduction and can range from 0.1 millidarcy to several darcys for conventional reservoirs (Eiken et al., 2011; Lie, 2019).

2.1.3 Representative Elementary Volume (REV)

A REV is basically a volume such that any rock samples the size of a REV will have physical properties almost identical to other rock samples in the neighbourhood. In other words, a REV is defined as a volume on which the chaotic behaviour of physical properties (e.g., porosity) on the microscopic level, due to the grain size distribution for instance, is averaged out.

Additionally, REV is also used to ensure that the continuum assumption for the fluid is applicable. Indeed, the distribution of fluids and rock particles is not continuous per nature but for a given scale (large enough to overpass the erratic microscopic level behaviour and small enough to still be treated as a volume element of continuum mechanics) they are relatively invariant so that the continuum assumption can be guaranteed.

Determining the appropriate volume, if it exists, depends on experiments on rock samples. If the focus is set on porosity, as displayed in Figure 2.1, the study focuses on porosity variations with samples of identical volume. For very small volume, on a microscopic level or below, samples can yield porosity in a wide range of values because some samples will be mostly composed of grains while other will be practically void. With growing sample volume, these high variations will slowly dampen out as the extreme porosity values encountered on a smaller scale will gradually cancel out each other. For a volume large enough, porosity will appear as constant over small regions. Such volumes are considered suitable for REV. For even larger scale, the risk of obtaining variations in the porosity

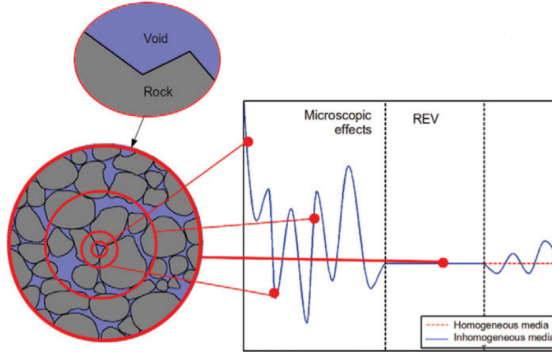


Figure 2.1: Search for an appropriate REV. In this case, porosity is the parameter used to determine the appropriate size for a REV (figure retrieved from (Lie, 2019)).

arises in heterogeneous media since some large regions of rocks may be composed of completely different rock type.

2.2 Single-phase flow

In the previous section, we introduced important notions that characterise porous media and on which reservoir engineers build their models. In the following section, we will detail the main laws governing the behaviour of a fluid in a single-phase environment.

2.2.1 Darcy's law

Henry Darcy was a hydraulic engineer who lived in France in the nineteenth century. He is known for experiments on single-phase flow in porous media (Darcy, 1856). More specifically, he designed a sand-filled tank that could let water flow through it and experiments on this tank led him to determine that the water flow rate Q [m^3/s] coming out of the tank was proportional to the tank's cross-sectional area A [m^2] and hydraulic head difference $h_t - h_l$ [m] and inversely proportional to the tank's length L [m]. Putting this into equation yields what is now known as Darcy's law for single-phase flow:

$$\frac{Q}{A} = \kappa \frac{h_t - h_l}{L}, \quad (2.3)$$

where κ is the hydraulic conductivity and has dimension $m \cdot s^{-1}$. A dimension analysis of the problem yields $\kappa = \rho g K / \mu$ with ρ [kg/m^3] the water density, g [m/s^2] the gravity acceleration, K [m^2] the permeability and μ [$kg/m/s$] the viscosity.

We now consider the left-hand side term of Equation (2.3) and see that its dimension is analogous to a speed. We then define $\vec{v} = Q/A$. However, \vec{v} is not a fluid velocity on the microscopic scale *per se* but rather can be seen as macroscopic velocity where we averaged the microscopic velocities of the fluid on a representative volume.

The name of Darcy's law for Equation (2.3) can also refer to a more common and "modern" continuous formulation given by

$$\vec{v} = -\frac{K}{\mu}(\nabla p - \rho g \nabla z). \quad (2.4)$$

It is also fairly common to introduce the notion of phase mobility as $\lambda = K/\mu$, although it mainly has utility in the case of multiple phase flow which we will be the subject of later discussions.

2.2.2 Single-phase problem formulation

With the help of the notion of REV established previously, the continuum assumption can be assumed valid and ensures that the fluid can be treated as continuous. Considering a defined control volume, called Ω , establishing the law of mass conservation over this domain yields the following

$$\frac{\partial}{\partial t} \int_{\Omega} \phi \rho \, d\vec{x} + \int_{\partial\Omega} \rho \vec{v} \cdot \vec{n} \, ds = \int_{\Omega} \rho q \, d\vec{x}, \quad (2.5)$$

where ϕ is the porosity, ρ [kg/m^3] the fluid density, v [m/s] the Darcy's velocity, n the outward normal of the surface $\partial\Omega$ of the control domain and q expresses the presence of sources or sinks of fluid within Ω . We then use the divergence theorem on the second term of Equation (2.5) so we can gather all the terms under a single integral operator

$$\int_{\Omega} \left(\frac{\partial(\phi\rho)}{\partial t} + \nabla \cdot (\rho \vec{v}) - \rho q \right) \, d\vec{x} = 0. \quad (2.6)$$

This equation remains true for any control volume Ω considered and in particular for infinitesimally small volumes. Thus, we get that the fluid must satisfy the following continuity equation

$$\frac{\partial(\phi\rho)}{\partial t} + \nabla \cdot (\rho \vec{v}) - \rho q = 0. \quad (2.7)$$

The introduction of additional assumptions will further simplify Equation (2.7). These assumptions will depend on the specifics of the study case, e.g. no fluid source or sink implying $q = 0$ or incompressible fluid which, when both combined, lead to the following

$$\nabla \cdot \vec{v} = 0, \quad (2.8)$$

2.3 Multiphase flow

In the previous section we defined Darcy's law and derived a problem formulation for a single-phase flow in a porous medium (e.g. an aquifer). However, in most cases, and especially in those we are interested in, more than one phase is present in reservoirs. For instance, oil reservoirs' pore space is expected to be packed with two or more phases: oil, water/brine and potentially gas, leading to a three-phase flow.

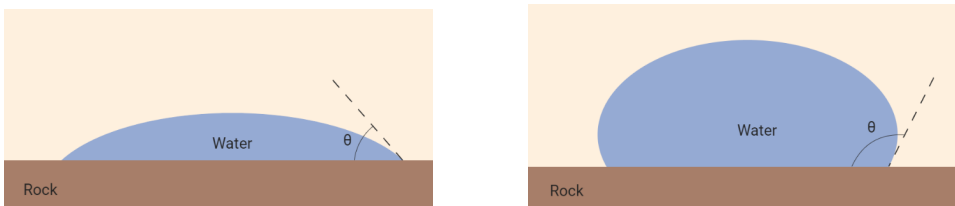


Figure 2.2: The wettability of a fluid influences the way it adheres to a solid interface through the contact angle θ . The right figure shows a water-wet system ($\theta \leq 90^\circ$) while the left figure depicts a non-water wet system ($\theta \geq 90^\circ$).

In the scope of this thesis, we take interest in the behaviour of CO_2 in aquifers or alternatively in depleted oil reservoirs. Hence, we will be considering a two-phase flow composed of an *immiscible* mix of water/brine and CO_2 .

The continuum assumption was postulated earlier in this chapter paired with the notion of REV. A consequence of this assumption is that any quantity evaluated at a given point in space \vec{x} actually refers to the average of the quantity on a neighbourhood with REV size around this point \vec{x} . It follows that although fluids are considered immiscible in the real physical world and perfectly separated by a thin interface, the pointwise average of fluid distribution may indicate a coexistence of the two entities at a given point. We must then define the saturation of each phase which is defined as the fraction of the volume occupied by that phase at a given point.

These saturations are denoted by the variables S_{water} and S_{CO_2} . For a phase α , S_α will take its values between 0 and 1, with $S_\alpha = 0$ meaning that phase α is absent and $S_\alpha = 1$ meaning the pores are completely filled with this phase. We also derive the following

$$S_{\text{water}} + S_{\text{CO}_2} = 1, \quad (2.9)$$

which is satisfied anywhere within the reservoir and at any time.

2.3.1 Wettability

Assuming we work with the immiscible hypothesis, the two phases will be separated by a thin interface. This interface is characterised by a surface tension representing the force necessary to modify its shape.

Wettability is the name given to the ability of a fluid to make and maintain contact with a solid interface (here, the reservoir's rock). Fluid flow will be affected by this parameter: if the interactions between the fluid and the rock induce strong adhesive forces, the flow will be slowed down.

When studying two distinct immiscible phases, one is more likely to create stronger adhesive forces with the rock. This phase will be called the *wetting* phase whereas the other is called *non-wetting* phase. Stronger adhesive forces are visually equivalent to a low contact angle between the phase and the solid interface as illustrated in Figure 2.2.

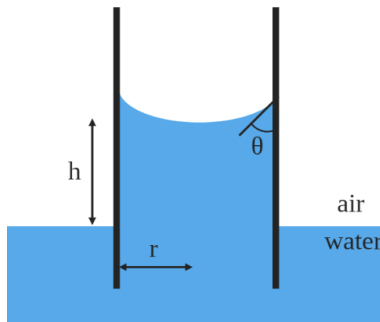


Figure 2.3: Tube invaded by a wetting fluid, here water, because of the capillary pressure.

From now on and for the rest of this thesis, subscript w refers to the wetting phase and subscript n refers to the non-wetting phase which we use to reformulate Equation (2.9) into

$$S_w + S_n = 1. \quad (2.10)$$

In many cases it has been observed that water acts as the wetting phase in aquifers and we will assume for later calculations that this is also the case along this thesis.

2.3.2 Capillary pressure

Capillary pressure is defined as the difference in phase pressures at the interface between two phases. This difference is generated by the surface tension and is expressed as the difference between the pressure in the non-wetting fluid and the pressure of the wetting fluid

$$p_c = p_n - p_w. \quad (2.11)$$

Overall, capillary pressure acts as an additional force that can force liquids to move into narrow spaces (often called capillary tubes) despite the action of other external forces such as gravity, see Figure 2.3.

Using the surface tension, we can derive that

$$p_c = \frac{2\sigma \cos(\theta)}{r}, \quad (2.12)$$

where σ is the surface tension, θ is the angle between the two phases at the solid or rock interface and r is the radius of the capillary tube. This also highlights that the wetting phase can invade smaller capillary tubes the higher the capillary pressure is.

Capillary pressure is often modelled as a saturation-dependent function (Lie, 2019) and thus

$$p_c = P_c(S_w). \quad (2.13)$$

2.3.3 Relative permeabilities

In Section 2.1.2, we have seen that the permeability K is a quantitative variable that depicts how fluids flow through porous media. Although K can depend on the state of the fluid (liquid or gaseous), on the type of rock and other parameters, we will here assume that these dependencies are negligible, and that the permeability is a piecewise constant and rock intrinsic function.

In the two-phase flow case, each fluid α will have its proper effective permeability K_α , which will necessarily be smaller than the absolute permeability K , intrinsic to the rock, which was used in the single-phase flow case. This is justified by the fact that the flow of one phase will be disturbed or slowed down by the presence of the other phase, which acts as an obstacle, and by the interactions happening at the interface between the two phases.

$$K_\alpha \leq K. \quad (2.14)$$

Relative permeability refers to the ratio between the effective permeability and the absolute permeability and is denoted $k_{r\alpha}$

$$k_{r\alpha} = \frac{K_\alpha}{K}. \quad (2.15)$$

Thanks to Equation (2.14), we know that the relative permeability takes its values in the interval $[0, 1]$. In some sense, it reflects the extent at which a fluid α flows optimally in the porous space. The closer $k_{r\alpha}$ is to 1, the more the effective permeability is close to the absolute permeability indicating that the phase α has almost perfect flow conditions.

The relative permeability is affected by numerous parameters including phase saturation, fluid's viscosity, rock's type, and pore-size distribution. However, for a domain modelled using a single rock type, it is often assumed that the relative permeabilities only depend on the phase saturation.

It is common to encounter more than a single rock type in underground reservoirs and they may each induce a different functional relationship between the relative permeability and the phase saturation. Hence, for heterogeneous media the relative permeability will be described as a function of both phase saturation and space, $k_{r\alpha} = k_{r\alpha}(S_\alpha, \vec{x})$. This also implies that relative permeabilities in homogeneous media can be given as functions of the saturation only: $k_{r\alpha} = k_{r\alpha}(S_\alpha)$.

Determining the exact functional relationship between the saturation of the wetting phase and the associated relative permeabilities for a given reservoir heavily relies on experiments on rock samples. These experiments aim at measuring apparent relative permeabilities for several values of saturation. The results are then used to find the function that fits best the data obtained. The literature provides (more than) a handful of existing models that have been derived from experiments on rock samples for various type of rocks and fluids (Lie, 2019, p 123). This diversity of derived models can now help engineers skip the experimentation process when the reservoir geological composition knowledge is considered sufficient.

This abundant source of models also shows that specific characteristics are shared by a large number of these models. For example, $k_{r\alpha}$ are often assumed to be continuous

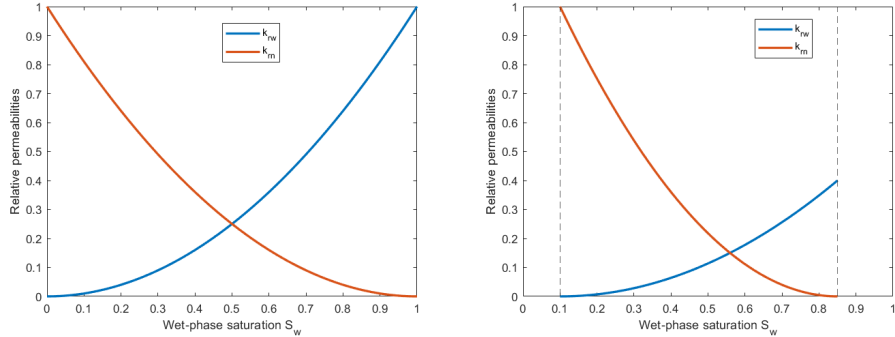


Figure 2.4: Examples of relative permeabilities for a two-phase system. The left graph shows a simple and ideal situation while the right graph represents a more realistic scenario taking into account residual saturations and their effects on the flow behaviour (pure Corey model).

monotone functions of saturation in homogeneous media, and increasing with S_α reflecting that the higher the saturation of a specific phase is, the easier this phase can move within the pore space of the reservoir.

For a two-phase flow, Equation (2.10) assures that the non-wetting phase saturation can always be derived from the wetting phase saturation: $S_n = 1 - S_w$. It is therefore fairly common in literature to give both relative permeabilities as functions of the wetting phase saturation, meaning that for the phase α we have $k_{r\alpha} = k_{r\alpha}(S_w)$.

The simplest and most common way to model relative permeabilities for a two-phase system is to define them using a power law of the saturation

$$k_{rw} = S_w^{n_w}, \quad k_{rn} = S_n^{n_n} = (1 - S_w)^{n_n}, \quad (2.16)$$

where the exponents n_w and n_n , also referred to as Corey exponents, are greater than 1. Relative permeabilities defined for $n_w = n_n = 2$ are given in the left graph of Figure 2.4.

From there, simplified and yet more accurate models are defined by taking into account other details such as residual saturation or adding a scaling factor (Lie, 2019). Relative permeabilities defined by such model can be found in the right graph of Figure 2.4.

For the rest of this thesis, in particular for later experiments and graphs, relative permeabilities will be given by Equation (2.16) with $n_w = n_n = 2$.

2.3.4 The fractional flow model

Our purpose here is to establish the model's ruling equations. All along this section we will mostly follow the main outline described in Lie (2019).

We start this section by using the mass conservation law for each of the two phases to

obtain two integral equations

$$\begin{aligned}\frac{\partial}{\partial t} \int_{\Omega} \phi \rho_w S_w \, d\vec{x} + \int_{\partial\Omega} \rho_w \vec{v} \cdot \vec{n} \, ds &= \int_{\Omega} \rho_w q_w \, d\vec{x}, \\ \frac{\partial}{\partial t} \int_{\Omega} \phi \rho_n S_n \, d\vec{x} + \int_{\partial\Omega} \rho_n \vec{v} \cdot \vec{n} \, ds &= \int_{\Omega} \rho_n q_n \, d\vec{x},\end{aligned}\tag{2.17}$$

which are both very similar to Equation (2.5) besides the first term where we took into account that the mass of a given fluid on a control volume is now a function of its saturation. Then, we follow the same pattern as what has been done in Section 2.2.2 to derive a continuity equation for each fluid

$$\begin{aligned}\frac{\partial}{\partial t} (\phi \rho_w S_w) + \nabla \cdot (\rho_w \vec{v}_w) &= \rho_w q_w, \\ \frac{\partial}{\partial t} (\phi \rho_n S_n) + \nabla \cdot (\rho_n \vec{v}_n) &= \rho_n q_n.\end{aligned}\tag{2.18}$$

These equations can be simplified when considering an incompressible flow in an incompressible porous medium, which is a fair assumption to make. These assumptions force ρ_α to be constant and indicate that ϕ remains constant over time for a given location. These additional constraints lead to the following set of equations

$$\begin{aligned}\phi \frac{\partial S_w}{\partial t} + \nabla \cdot \vec{v}_w &= q_w, \\ \phi \frac{\partial S_n}{\partial t} + \nabla \cdot \vec{v}_n &= q_n.\end{aligned}\tag{2.19}$$

With the help of Equations (2.4) and (2.15), we introduce the notion of phase-wise Darcy velocity as well as total Darcy velocity as follow

$$\vec{v}_\alpha = -\frac{K k_{r\alpha}}{\mu_\alpha} (\nabla p_\alpha - \rho_\alpha g \nabla z),\tag{2.20a}$$

$$\vec{v} = \vec{v}_w + \vec{v}_n.\tag{2.20b}$$

We now define properly the notion of phase mobility that had been evoked earlier in Section 2.2.1 so that it takes into account the relative permeability, namely $\lambda_\alpha = \lambda_\alpha K = K k_{r\alpha} / \mu_\alpha$, and define the total mobility λ and total relative mobility λ_r as $\lambda = \lambda_w + \lambda_n = \lambda_r K$. These notations are used to simplify the partial darcy velocities derived from Darcy's law in (2.20a) into

$$\vec{v}_\alpha = -\lambda_\alpha K (\nabla p_\alpha - \rho_\alpha g \nabla z).\tag{2.21}$$

Then, we multiply each relative phase mobility by the velocity from the opposite phase, subtract the results, and use Equation (2.21) to get

$$\begin{aligned}\lambda_n \vec{v}_w - \lambda_w \vec{v}_n &= -\lambda_n \lambda_w K (\nabla p_w - \rho_w g \nabla z) - (-\lambda_w \lambda_n K (\nabla p_n - \rho_n g \nabla z)) \\ &= \lambda_w \lambda_n K (\nabla p_c + \Delta \rho g \nabla z),\end{aligned}\tag{2.22}$$

where $\Delta\rho = \rho_w - \rho_n$ and p_c is the capillary pressure as defined earlier, $p_c = p_n - p_w$. We notice that we also have $\lambda_n \vec{v}_w - \lambda_w \vec{v}_n = \lambda \vec{v}_w - \lambda_w \vec{v}$ and use this equality to isolate \vec{v}_w and get

$$\vec{v}_w = \frac{\lambda_n \vec{v}_w - \lambda_w \vec{v}_n}{\lambda} + \frac{\lambda_w}{\lambda} \vec{v}. \quad (2.23)$$

Then, we replace the numerator of the first term on the right-hand side of this equation by what has been obtained in Equation (2.22) and insert this new expression of \vec{v}_w into the first equation of (2.19) to get the *saturation equation*

$$\phi \frac{\partial S_w}{\partial t} + \nabla \cdot (f_w \vec{v} + f_w \lambda_n K \Delta \rho g \nabla z) = q_w - \nabla \cdot (f_w \lambda_n K P'_c \nabla S_w), \quad (2.24)$$

with $f_w = \lambda_w / \lambda = \lambda_w / (\lambda_n + \lambda_w)$, the fractional flux function, and where we used Equation (2.13) to derive $\nabla p_c = P'_c \nabla S_w$. Equation (2.24) is very often simplified into the following equation

$$\phi \frac{\partial S_w}{\partial t} + \nabla \cdot (f_w \vec{v} + f_w \lambda_n K \Delta \rho g \nabla z) = 0. \quad (2.25)$$

when there are no production wells nor injection in the reservoir, i.e. $q_w = 0$, and capillary pressure effects are negligible.

2.4 Analytical solutions for 1D flow

To get a better insight on the flow behaviour occurring in a reservoir, a set of examples with particular conditions in which analytical solutions can be reached with a certain degree of ease is laid out.

Capillary pressure will be neglected for simplicity. Let us also simplify some notation to make it easier for the reader:

- The saturation of the wetting phase will be referred to as S , without its former subscript w .
- Similarly, a notation and name simplification will be performed on the fractional flux function f_w which we will refer to as f or *flux function* from now on.
- Lastly, Darcy's velocities are scalar quantities in 1D and will hence be referred to without their original vector notation.

2.4.1 A first approach in horizontal homogeneous media

The first study case considered is the horizontal medium. Due to this configuration, gravity forces will have no impact on the flow behaviour leading to a first problem simplification.

The total flux velocity v is originally defined as the sum of the two partial flux velocity, see Equation (2.20b). Therefore, summing the two equations given in Equation (2.19) and

using Equation (2.10), which states that the sum of the saturations is constant (equal to 1), yields a simplified version of the *pressure equation*

$$v'(x) = q(x). \quad (2.26)$$

In particular, this means that the total velocity v is constant in the absence of source terms. Assuming that flow is driven entirely by boundary conditions and that no source term is active, a new formulation for the saturation equation can be derived and is given by

$$\phi \frac{\partial S}{\partial t} + v \frac{\partial f}{\partial x} = 0. \quad (2.27)$$

For simplicity purpose and without loss of generality, v/ϕ is assumed equal to 1. This can be accomplished by rescaling the time parameter t .

$$\frac{\partial S}{\partial t} + \frac{\partial f(S)}{\partial x} = 0. \quad (2.28)$$

Equation (2.28), also called the *Buckley-Leverett* equation, is provided with some initial condition $S(x, 0) = S_0(x)$ (and additional boundary condition if needed), to ensure the well-posedness of the problem.

We solve this equation at first hand using the method of characteristics. We define $x(t)$ a trajectory such that $S(x(t), t) = S(x(t_0), t_0)$ for any $t \geq t_0$. For such a characteristic line, the differentiation of S yields

$$dS = \frac{\partial S}{\partial t} dt + \frac{\partial S}{\partial x} dx = 0.$$

On the other hand, f can be described as a function of S only and thus

$$\frac{\partial f(S)}{\partial x} = \frac{\partial f}{\partial S} \frac{\partial S}{\partial x},$$

which can be combined with the previous differentiation for S to obtain

$$\begin{aligned} \frac{\partial S}{\partial x} \left(\frac{dx}{dt} \right) \Big|_{dS=0} &= \frac{\partial f}{\partial S} \frac{\partial S}{\partial x}, \\ \implies \frac{dx}{dt} \Big|_{dS=0} &= \frac{\partial f}{\partial S}. \end{aligned} \quad (2.29)$$

Then, the trajectory of a particle remaining on a line of constant saturation is given by a simple integration of Equation (2.29) over time

$$x(t) = x_0 + (t - t_0) \frac{\partial f}{\partial S}(S_0), \quad (2.30)$$

where $x_0 = x(t_0)$ is the initial position of the characteristic trajectory and $S_0 = S(x_0, t_0)$ is the saturation at the initial time for the trajectory $x(t)$.

For simple cases where the flux function is given as a linear function of the saturation, i.e. $f(S) = S$, one can easily determine that the saturation profile at any time. Let the porous

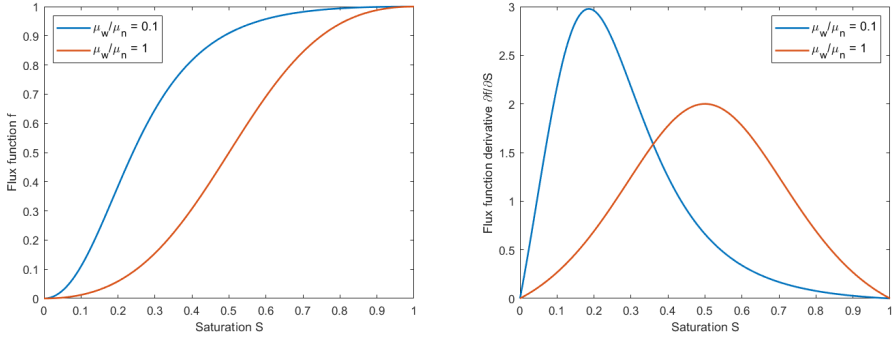


Figure 2.5: Flux function f and its derivative as functions of the saturation. Two curves, each based on a different viscosity ratio, are displayed for better illustration of the impact of this ratio on the fractional flux function.

medium be defined on $] -\infty; +\infty[$, then the saturation is given by $S(x, t) = S_0(x - t)$. This example denotes a simple propagation of the information along the x-axis with unit speed.

In the current study case however, the flow function f is given by

$$f(S) = \frac{\lambda_w(S)}{\lambda_w(S) + \lambda_n(S)} = \frac{\frac{k_{rw}(S)}{\mu_w}}{\frac{k_{rw}(S)}{\mu_w} + \frac{k_{rn}(S)}{\mu_n}}.$$

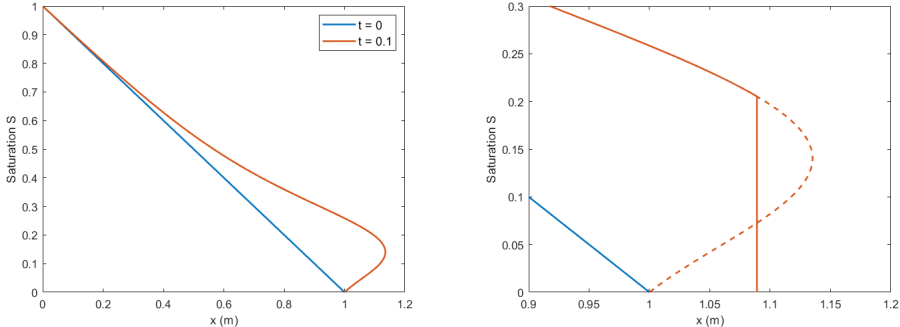
More specifically, the explicit form of f and its derivative are

$$f(S) = \frac{S^2}{S^2 + \frac{\mu_w}{\mu_n}(1-S)^2}, \quad (2.31)$$

$$\frac{\partial f}{\partial S}(S) = \frac{2\frac{\mu_w}{\mu_n}S(1-S)}{(S^2 + \frac{\mu_w}{\mu_n}(1-S)^2)^2}. \quad (2.32)$$

The left graph of Figure 2.5 displays two possible flux function depending on the value of the viscosity ratio μ_w/μ_n while the graph on right depicts their respective derivative.

Note that f' has an isolated extremum attained a saturation value \tilde{S} or equivalently that f has an inflection point. Looking back at Equation (2.30), the method of characteristics derived that the speed of characteristic lines is proportional to the derivative of f . In particular this means that characteristic lines for saturation values that are near the extremum \tilde{S} will have a much higher speed than lines obtained for saturation values near 0 or 1 where the derivative of f is almost equal to 0. Thus, the use of the method of characteristics can easily provide us with examples where the saturation becomes a multivalued function after a finite amount of time regardless of the continuity properties of the initial data.



(a) Saturation profile evolution in time according to the method of characteristics.

(b) Construction of a discontinuity preserving the fluid's mass.

Figure 2.6: Emergence of a multivalued saturation profile after a finite time of simulation. This non-physical behaviour is handled by constructing a discontinuity. The flux functions used here have been computed with $\mu_w/\mu_n = 0.1$.

For instance, consider the case where we have a medium given on the domain $[-\infty, \infty[$ and where the initial saturation is given by

$$S(x, 0) = S_0(x) = \begin{cases} 1, & x \leq 0, \\ 1 - x, & 0 \leq x \leq 1, \\ 0, & x \geq 1. \end{cases}$$

We compute the speed of the characteristic lines of constant saturation and then determine their position in time as the method of characteristics would give them. Figure 2.6a displays the saturation profile obtained after a given time $t > 0$. The function is multivalued as expected, and is non-physical. Hence, the next step is to find a way to make it physically acceptable.

The way to bypass this non-physical situation is to consider a discontinuity in the saturation profile (dark-orange plain line on the right graph of Figure 2.6b) instead of this continuous profile we had beforehand. The discontinuity constructed needs to preserve the fluid's mass. This is done by ensuring that the mass of fluid cut by the discontinuity equals the fluid's mass added under the dashed curve.

Graphically, the discontinuity simply sits at the point where the area on the right of the discontinuity is equal to the area on the bottom left hand side of the discontinuity.

Nonetheless, introducing a discontinuity in our saturation solution means that the pointwise existence of the derivative can no longer be guaranteed.

Since potential physical solutions might no longer meet the continuity requirement for the original saturation equation (2.28), weak solutions must be defined instead. This is achieved by multiplying the saturation equation by a test function Φ , which is both smooth

and with compact support, and then integrating the outcome over space and time

$$\iint \left(\frac{\partial S}{\partial t} + \frac{\partial f(S)}{\partial x} \right) \Phi(x, t) \, dx dt = 0.$$

An integration by part will have the smooth function Φ bear the derivatives. It yields

$$\iint \left(S \frac{\partial \Phi}{\partial t} + f(S) \frac{\partial \Phi}{\partial x} \right) \, dx dt = \int_{\mathbb{R}} S_0(x) \Phi(x) \, dx. \quad (2.33)$$

Weak solutions are now given by functions S that verify Equation (2.33) for any test function Φ .

Beyond the graphical analysis from Figure 2.6b, discontinuities that occur in these weak solutions are subject to particular conditions shown below.

For instance, consider a discontinuity whose trajectory is given by $x_d(t)$ and consider a and b , two points such that $a < x_d < b$. Let S_a , respectively S_b , be the saturation at a , respectively at b . We also denote by S^+ , respectively S^- , the saturation immediately ahead, respectively behind, the discontinuity curve. Integrating the saturation equation (2.28) from a to b reads

$$\frac{d}{dt} \int_a^b S(x, t) \, dx = - \int_a^b \frac{\partial f(S)}{\partial x} \, dx = f(S_a) - f(S_b). \quad (2.34)$$

Then we decompose the integral on the left-hand side of the equation into two in integrals each defined on one side of the discontinuity and where the end points at the discontinuity are given as limits:

$$\int_a^b S(x, t) \, dx = \lim_{\epsilon \rightarrow 0^+} \int_a^{x_d(t)-\epsilon} S(x, t) \, dx + \lim_{\epsilon \rightarrow 0^+} \int_{x_d(t)+\epsilon}^b S(x, t) \, dx. \quad (2.35)$$

The integrand, $S(x, t)$, is continuous on both subintervals and hence the Leibniz rule can be applied to both integrals. Calculations are expressed for the integral defined on the left of the discontinuity, but calculations on the right hand-side give similar results thanks to symmetry.

$$\frac{d}{dt} \lim_{\epsilon \rightarrow 0^+} \int_a^{x_d(t)-\epsilon} S(x, t) \, dx = \lim_{\epsilon \rightarrow 0^+} \int_a^{x_d(t)-\epsilon} \frac{\partial S}{\partial t} \, dx + \frac{dx_d}{dt} S(x_d(t) - \epsilon, t).$$

Letting a tend to $x_d(t) - \epsilon$ forces the first term on the right-hand side to fade away. Introducing this result in Equation (2.34) and taking the limit as ϵ tends to 0 yields

$$\frac{dx_d}{dt} (S^+ - S^-) = f(S^+) - f(S^-), \quad (2.36)$$

also known as the Rankine-Hugoniot condition where dx_d/dt , commonly referred to as σ , is the speed of the discontinuity curve (Lie, 2019).

Although discontinuities from weak solutions to Equation (2.33) will necessarily verify the Rankine-Hugoniot jump condition, there is not enough constraints to guarantee that these weak solutions are physically admissible yet.

Entropy conditions are an additional set of requirements that a discontinuity must satisfy to induce a physically relevant weak solution. For flux functions that are strictly convex, the appropriate form of the entropy condition is the Lax Entropy condition given by

$$f'(S^-) > \sigma > f'(S^+). \quad (2.37)$$

This condition can be seen as a way to enforce that waves from the immediate left of the discontinuity, i.e. behind it, move faster than the discontinuity which itself progresses faster than waves from immediate neighbourhood on the right of the discontinuity. In other words, the Lax Entropy condition prevents the selection of discontinuities where the waves ahead or behind the discontinuity would tear it apart. Discontinuities meeting this requirement are called *shock waves*.

One can also note that there will be a single physically admissible solution to the weak problem formulation (2.33) whose shock waves satisfy both the Rankine-Hugoniot jump condition (2.36) and the entropy solution (2.37).

However, in cases where the flux function is not convex (nor concave), the Lax entropy condition must be generalised to a broader version of the entropy condition called Oleinik entropy condition which asserts that any discontinuity for physical solution must satisfy

$$\frac{f(S) - f(S^-)}{S - S^-} > \sigma > \frac{f(S) - f(S^+)}{S - S^+}, \quad (2.38)$$

where S takes its values in the interval between S^- and S^+ .

Let us now consider a Riemann problem, a conservation equation paired with an initial condition piecewise constant with a single discontinuity, given by

$$\begin{cases} \frac{\partial S}{\partial t} + \frac{\partial f(S)}{\partial x} = 0, & t \geq 0, x \in \mathbb{R}, \\ S(0, x) = S_0(x), \end{cases} \quad (2.39)$$

where $S_0(x)$ is a piece-wise constant function with $S_0(x) = S_L$ for $x < 0$ and $S_0(x) = S_R$ for $x > 0$.

For f uniformly convex, an admissible solution has two possible evolution in time.

If $S_L > S_R$, the Lax Entropy condition is satisfied since f is uniformly convex. Hence the previous discussion ensures that the solution will propagate the shock along the x-axis with speed by determined the Rankine-Hugoniot condition.

If $S_L < S_R$, we have $f'(S_L) < f'(S_R)$, indicating that the Lax Entropy condition cannot be verified and in particular, particles located ahead of the discontinuity at initial time have greater speed than those located behind it. On the characteristic plane this would be equivalent to the creation of an area where the characteristic lines are undefined. The

solution to this Riemann problem will introduce a Riemann fan in the characteristic plane between the lines $(tf'(S_L), t)$ and $(tf'(S_R), t)$ and is given by

$$S(x, t) = \begin{cases} S_L, & f'(S_L) \leq x/t, \\ (f')^{-1}(x/t), & f'(S_L) < x/t < f'(S_R), \\ S_R, & x/t > f'(S_R). \end{cases} \quad (2.40)$$

Note that this solution is continuous after a finite amount of time despite being formed from initial discontinuous condition.

For flux functions that are not convex (e.g., flux functions given in Figure 2.5), there still exists a convenient way to determine the solution based on the use of *upper concave* envelope of f , or *lower convex* envelope depending on the context.

The upper concave envelope can be constructed graphically using a rubber band. Place a rubber band above the graph of f and enforce the two ends of the rubber band to sit at $(S_L, f(S_L))$ and $(S_R, f(S_R))$. The shape defined by the rubber band will correspond to the upper concave envelope of f between S_R and S_L . The function describing the path taken by the rubber band is referred to as f_c to follow notation used in Lie (2019). By definition $f_c'' < 0$. The lower convex envelope is defined similarly by enforcing the rubber band on the graph of f between S_L and S_R from below.

The solution to the Riemann problem with f non necessarily convex is given by the following

$$S(x, t) = \begin{cases} S_L, & x/t < f'_c(S_L), \\ (f'_c)^{-1}(x/t), & f'_c(S_L) < x/t < f'_c(S_R), \\ S_R, & x/t > f'_c(S_R), \end{cases} \quad (2.41)$$

where f_c denotes the upper concave envelope if $S_L > S_R$ and symmetrically denotes the lower convex envelope if $S_L < S_R$ (Lie, 2019; Holden and Risebro, 2002). The literature credits Welge (1952) for the graphical construction of such a solution.

We illustrate this with an example. Consider the Riemann problem given in (2.39) with initial saturations values given as $S_L = 1$ and $S_R = 0$. Then the solution can be computed by looking at the concave hull of f which is displayed in Figure 2.7.

From left to right on the graph, we see that the hull is linear at first from the $S_R = 0$ until S^* , and then it follows the curve of f until $f_L = 1$. Hence a shock wave is generated from the origin and moves to the right with saturation below the shock wave equal to S^* while a rarefaction wave stretches between the shock and the origin.

2.4.2 Flow in vertical homogeneous media

Consider now a vertical porous medium. The saturation equation, given in Equation (2.25), is rewritten along the z-axis and reads

$$\phi \frac{\partial S}{\partial t} + \frac{\partial(fv)}{\partial z} + \frac{\partial}{\partial z}(f\lambda_n K \Delta\rho g) = 0. \quad (2.42)$$

We assume without generality loss that $\Delta\rho$ is not equal to 0, or equivalently that fluids have different density. Fluids' movement on the vertical axis are mostly driven by the

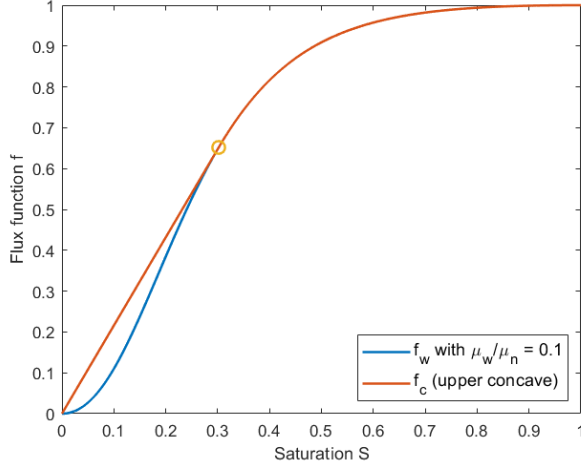


Figure 2.7: Flux function for horizontal 1D displacement and its concave hull between 0 and 1. The circle marker denotes the saturation at which a rarefaction to a shock.

gravity segregation and hence the impacts of advection are neglected with respect to those of gravity, meaning that the second term of the previous equation is considered negligible.

Additionally, the constant $K\Delta\rho g/\phi$ is scaled away to obtain a more appealing version of the saturation equation, given as follow

$$\frac{\partial S}{\partial t} + \frac{\partial(f\lambda_n)}{\partial z} = 0. \quad (2.43)$$

For the sake of notation simplification, the flux function governing gravity segregation $f\lambda_n$ is renamed to f_g . A more complete expression of f_g is given by

$$f_g(S) = \frac{\lambda_w(S)\lambda_n(S)}{\lambda_w(S) + \lambda_n(S)} = \frac{\frac{k_{rw}(S)}{\mu_w} \frac{k_{rn}(S)}{\mu_n}}{\frac{k_{rw}(S)}{\mu_w} + \frac{k_{rn}(S)}{\mu_n}}.$$

If we consider the case where the relative permeabilities of each fluid are given as the square of their respective saturation, i.e. that $n_w = n_n = 2$, we then have that

$$f_g(S) = \frac{1}{\mu_n} \frac{S^2(1-S)^2}{S^2 + \frac{\mu_w}{\mu_n}(1-S)^2}. \quad (2.44)$$

This flux function is characterised by its bell shape function: it keeps the same sign on $[0, 1]$ with $f_g(0) = f_g(1) = 0$ and has a single extremum on $]0, 1[$. Although it has been scaled away, $\Delta\rho$ still impacts the flow behaviour through its sign. We denote this influence by letting the bell shape point upward if $\Delta\rho$ is positive and downward if $\Delta\rho$ is negative. Water is denser than CO₂, and therefore further examples will illustrate situations where $\Delta\rho$ is positive. The flux function with bell-shape as defined in Equation (2.44) is given

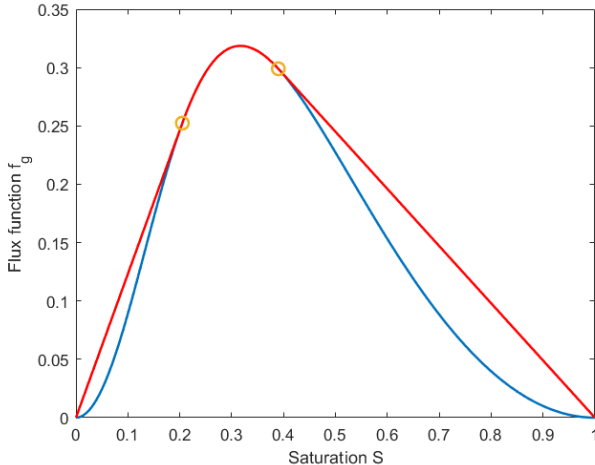


Figure 2.8: The gravity segregation flux function, in blue, and its upper concave envelope between 0 and 1. The relative permeabilities are computed as described in Equation (2.16) with Corey-exponents $n_w = n_n = 2$ and we set $\mu_w/\mu_n = 0.1$.

in Figure 2.8. Here again, following purely the method of characteristics would lead us to non-physical solutions. Thus, the solution for a given Riemann problem is determined thanks to Equation (2.41).

We illustrate the construction of the Riemann solution with the following example (also see Example 8.4.2 in Lie (2019)). Consider a porous medium, a vertical one-dimensional column bounded by above and below. The domain is given by $[0, 1]$ for simplicity, though it can always be scaled if needed. Furthermore, assume that both fluids are perfectly separated, each filling completely their own half of the reservoir with a fluid interface at $z = 0.5$, representing the situation where one fluid sits on top of the other.

If the lighter fluid, here CO_2 , sits on top of the other fluid, here water, we expect that nothing happens. In this case, $S_L = S(z = 0.5^-, 0) = 0$ and $S_R = S(z = 0.5^+, 0) = 1$, and thus $S_L < S_R$ and the Riemann solution is given by the upper concave envelope. Since f_g is positive with $f_g(0) = f_g(1) = 0$, the envelope corresponds to a single straight line from $(1,0)$ to $(0,0)$, corresponding to a stationary shock (the slope of the line is 0). In brief, nothing happens which is what was expected.

If the lighter fluid lies below, then the upper concave envelope needs to be computed to determine the solution of the Riemann problem. The upper concave envelope is shown in Figure 2.8. Linear parts of the envelope indicate the formation and propagation of a shock wave while parts of the envelope that overlap the graph of f_g denote a rarefaction wave. Here, we see that the concave hull follows three distinct states. It is first linear from $S_R = 0$ to a saturation value $S^+ \approx 0.2$, then follows the graph of f_g until saturation reaches $S^- \approx 0.39$ and finally it is linear from S^- back to S_L .

Hence from the original state, a shock wave moves to the right of the z-axis with saturation ahead and behind given by $S_R = 0$ and $S^+ \approx 0.2$ with speed corresponding to the slope of the linear first part of the envelope (see Equation (2.36)). Another shock wave moves leftward with speed and saturation above and below obtained similarly. Finally, a rarefaction wave generates a smooth saturation transition from S^- to S^+ . Based on this information and Equation (2.41), we can describe the saturation profile solution for the Riemann problem right after the initial state. with regions filled with a single-phase type on the end of the reservoir and an expanding two-phase region in the middle as the shocks move away from the centre of the reservoir. Note that this description holds as long as none of the shock hit one of the wall of the reservoir.

When that happens, it gives birth to additional Riemann problems which are interesting to look at. We refer to Example 8.4.2 in Lie (2019) which provides a detailed description of the behaviour of the solution when these shock waves reach the boundaries of the reservoir.

2.4.3 Flow in inhomogeneous vertical media

In the two previous subsections, the considered medium was formed of a homogeneous rock, meaning the geophysical parameters of the rock were assumed constant within the domain. In particular, this meant that the flux functions f and f_g were given as constant functions of space.

In this subsection, although we continue to focus on a vertical porous medium, we will now assume that the flux function has a space discontinuity. Say for instance that the media is divided in two by an interface at $z = 0$ and that the flux function on the right side of this interface is f^+ while the left side flux is f^- with $f^+ \neq f^-$.

Changes in the rock composition or grain size distribution can cause this flux function function discontinuity. Although their impacts can vary, they are mostly translatable into modifications in the relative permeabilities profile, as already mentioned in Section 2.3.3 and/or heterogeneity in permeability fields.

The saturation equation for a vertical medium is given in Equation (2.42). We once again, neglect advection compared to the gravity segregation and scale away the constant $\Delta\rho g/\phi$ (note that K is not part of the scaled constant this time) to get following Riemann problem with discontinuous flux functions

$$\begin{cases} \frac{\partial S}{\partial t} + \frac{\partial}{\partial z}(K\lambda_n f_d) = 0, \\ S(x, 0) = S_0(x), \end{cases} \quad (2.45)$$

with $f_d = f^-\mathbb{1}_{x<0} + f^+\mathbb{1}_{x>0}$.

As exposed in this thesis' introduction, we focus only on heterogeneous permeability fields. Hence, relative permeabilities profile are assumed unchanged through the interface, only the absolute permeability induces a discontinuity in the flux function.

For now, we define the permeability as a piece-wise constant function with a single dis-

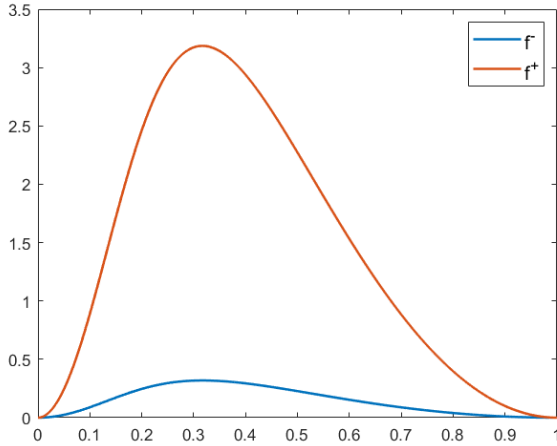


Figure 2.9: Comparison of the flux functions defined on each side of the origin. Here we defined the permeabilities of each side of the interface as $K^- = 1$ and $K^+ = 10$.

continuity at the origin (or equivalently at the middle of the reservoir), i.e.

$$K(z) = \begin{cases} K^-, & z < 0, \\ K^+, & z > 0. \end{cases} \quad (2.46)$$

The new flux functions f^+ and f^- are given by

$$f^\pm(S) = (K^\pm \lambda_n f)(S). \quad (2.47)$$

Thus, we have that $f^+ = K^+/K^- \times f^-$ which indicates that f^+ is a scaled version of f^- . Figure 2.9 depicts the two flux functions for $K^- = 1$ and $K^+ = 10$.

As already discussed in the previous sections, a solution to the problem (2.45) is likely to be/become discontinuous after a finite time. Hence, we look for weak solutions of the problem that satisfy

$$\iint_{\mathbb{R}^+ \times \mathbb{R}} S \Phi_t \, dx dt + \iint_{\mathbb{R}^+ \times \mathbb{R}} f_d(S) \Phi_x \, dx dt + \int_{\mathbb{R}} S_0(x) \Phi(0, x) \, dx = 0, \quad (2.48)$$

where Φ is a smooth function with compact support. We also have that S is a solution of (2.48) if and only it is also solution to the following

- S is a weak solution of (2.45) on each side of the origin for all $t > 0$,
- S satisfies $S(0, x) = S_0(x)$ for $x \in \mathbb{R}$,
- $f^+(S^+(t)) = f^-(S^-(t))$ for almost all $t > 0$ where the saturation values $S^\pm(t)$ are defined as $S^\pm(t) = \lim_{x \rightarrow 0^\pm} S(x, t)$. This last condition is referred to as the *interface Rankine-Hugoniot condition* and expresses the conservation of mass across the frontier.

In Section 2.4.1, we defined an entropy condition, namely the Oleinik entropy condition, given in Equation (2.38) which guaranteed the uniqueness of the solution of (2.28). Because of the flux function discontinuity, this same entropy condition is no longer sufficient to single out a unique solution to the problem (2.45). We still enforce it away from the interface but an additional entropy condition at the interface itself is necessary to guarantee uniqueness of the solution in the general case.

However, for our particular study case, the flux function discontinuity at the interface is caused by a discontinuity in the permeability. The relative permeabilities are left untouched across the interface. Hence, the flux functions on each side of the interface are scaled version of each other, as already mentioned and described in Figure 2.9. This implies that f^+ and f^- do not intersect on $]0, 1[$.

This allows us to compute the solution of the Riemann problem with discontinuous flux function (2.45) without enforcing a supplementary entropy condition at the interface.

Consider the Riemann problem (2.45) with initial data given by

$$S(x, 0) = S_0(x) = \begin{cases} S_L = 1, & z < 0, \\ S_R = 0, & z > 0, \end{cases} \quad (2.49)$$

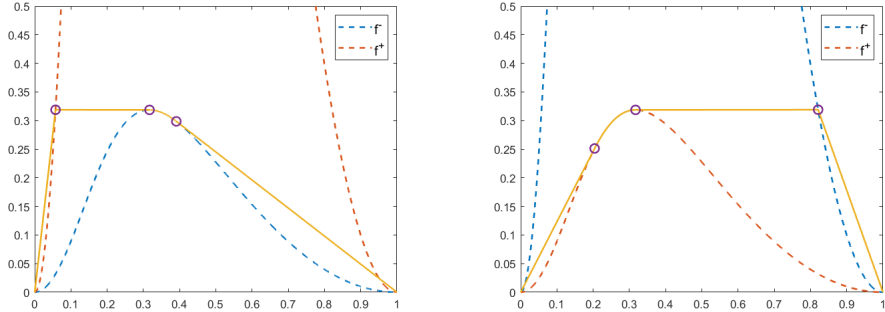
and with discontinuous flux function given by Equation (2.47). We first look at the case where $K^- < K^+$ which physically represents the situation where the lower permeable region is on top of the higher permeable region.

The unique solution respecting the Oleinik entropy condition and the interface Rankine-Hugoniot condition is given in Figure 2.10a. Because $S_R = 0$, it is necessarily smaller than S^+ , the saturation at the below interface, hence we compute the concave hull of f^+ between S_R and S^+ . For the same reasons, we solution in the upper region is computed using the upper concave envelope of f^- between S^- and S_L . From left to right on the graph, the solution is determined by a downward moving shock with saturation below and above given by $S_R = 0$ and $S^+ \approx 0.058$, a stationary shock at the interface with saturation above $S^- \approx 0.32$, a rarefaction wave and an upward moving shock with saturation below and above given by $S_L^* \approx 0.39$ and $S_L = 1$.

In the event where the region of lower permeability is actually below the interface, $K^- > K^+$, the solution computed is given in Figure 2.10b. A similar analysis yields that the solution is determined a downward moving shock in the lower region with saturation below and above given by $S_R = 0$ and $S_R^* \approx 0.21$, a rarefaction wave, a stationary shock at the interface with saturation below and above given by $S^+ \approx 0.32$ and $S^- \approx 0.82$, and an upward moving shock with saturation below and above given by $S^- \approx 0.82$ and $S_L = 1$.

We could also consider the case where the lighter fluid, here CO_2 , lies above the water, i.e. $S_0(x) = \mathbb{1}_{x>0}$. In this scenario, the solution would be computed on each side of the region using the lower convex envelope which is given by a straight horizontal line indicating a stationary shock at the interface. Nothing happens, each phase remains in their respective region.

So far, it was assumed that only permeability was discontinuous across the interface and that relative permeabilities were identical in each region. However, permeability hetero-



(a) The region with lower permeable rock lies above the interface. (b) The region with lower permeable rock lies below the interface.

Figure 2.10: Comparison of the Riemann solution obtained for 2 different scenarios. In both cases, the water lies above the interface in the region with negative z (the z-axis points downward). The region with lower permeability is alternatively place above the interface and below.

genetics are often caused by changes in the rock type (grain size distribution, type of sediments, etc.) and such changes are likely to affect the relative permeabilities too which in turn will cause additional perturbations in the flux functions. Specifically, we may end-up with flux functions that intersect. Then the solution to the Riemann problem with discontinuous flux function (2.45) can no longer be uniquely defined by the process used in Figure 2.10. In this type of situations, the additional entropy condition at the interface mentioned earlier must be defined to guarantee the uniqueness of the solution.

The choice for the entropy condition at the interface has been an extensively studied topic throughout the last three decades. A literature review is out of the scope of this thesis but we refer the reader to several articles defining or describing some specific entropy conditions.

The *minimal jump condition* was first derived by Gimse and Risebro (1991) (see also Gimse and Risebro (1992)). This method essentially defines an entropy condition that enforces the saturation jump at $x = 0$, denoted by $|S^+ - S^-|$, to be minimal. It was also proven that this method is equivalent to the *vanishing viscosity method* which consists in viewing the differential equation in (2.45) as the limit of $S_t + [f_d(S)]_x = \varepsilon S_{xx}$ as ε tends to 0.

Using a similar idea, Langtangen et al. (1992) derived an entropy inequality by viewing (2.45) as the limit of a parabolic equation with a diffusion term

$$\frac{\partial S_\varepsilon}{\partial t} + \frac{\partial f_d(S_\varepsilon)}{\partial x} = \varepsilon \frac{\partial^2 S_\varepsilon}{\partial x^2}.$$

This was later completed by (Kaasschieter, 1999) which replaced the diffusivity term by the capillary diffusion given as follows

$$\frac{\partial S_\varepsilon}{\partial t} + \frac{\partial f_d(S_\varepsilon)}{\partial x} = \varepsilon \frac{\partial}{\partial x} \left(f_d(S_\varepsilon) \frac{\partial}{\partial x} P_c(S_\varepsilon) \right). \quad (2.50)$$

Chapter 3

MRST and model set-up

3.1 MATLAB Reservoir Simulation Toolbox (MRST)

MRST is an open-source software developed at SINTEF Digital and primarily focusing on reservoir modelling and simulation (Lie, 2019). It is designed to provide the user with a great number of modules and functions to help them create, build, or use existing models of porous media or reservoirs as well as developing new simulation methods.

This thesis' experiments were conducted using the Version 2019b of MRST, and more specifically, the module *incomp*. Fluids are indeed assumed incompressible in this thesis as described in the model set-up in Section 3.2.

3.1.1 The Two-Point Flux Approximation (TPFA)

The solver used for the simulations is based on the TPFA method which is a finite-volume discretisation method. We do not explicit all the details on how to derive the method here and we rather focus on giving general results leading to the definition of the transmissibility field. We refer the reader to additional literature for more details, justifications, comments, and limitations of the method (see Lie, 2019, Section 4.4.1).

Consider Ω_i and Ω_j , two cells in a grid sharing a common face. Looking at Ω_i , the Darcy flux across this shared face is defined as

$$v_{i,j} = \int_{\Gamma_{i,j}} \vec{v} \cdot \vec{n}_{i,j} \, ds, \quad \Gamma_{i,j} = \partial\Omega_i \cap \partial\Omega_j, \quad (3.1)$$

where $\vec{n}_{i,j}$ is the outward normal from Ω_i on the shared face, $\Gamma_{i,j}$, which is called a *half-face* and has associated area $A_{i,j}$. The considered grid is assumed to have matching faces and thus, we have $\vec{n}_{i,j} = -\vec{n}_{j,i}$ and $A_{i,j} = A_{j,i}$.

From there, we approximate the integral using the mid-point rule and use Darcy's law to get

$$v_{i,j} \approx -A_{i,j} \left(\frac{K \nabla p}{\mu} \right) (\vec{x}_{i,j}) \cdot \vec{n}_{i,j}, \quad (3.2)$$

with $\vec{x}_{i,j}$, the centroid of $\Gamma_{i,j}$.

Evaluating the gradient can be performed with a one-sided finite difference between the pressure at the face centroid, given by $p(\vec{x}_{i,j}) = \pi_{i,j}$, and at another point in the cell. In finite-volume method, pressure is defined as a cell average quantity and hence there is no direct point in the cell to use for the gradient evaluation. However, if the pressure is assumed linear inside the cell, the pressure at the centre of the cell is exactly the average cell pressure p_i . If we let $\vec{c}_{i,j}$ denote the vector from the centre of the cell and the face centroid, this one-sided difference is then approximated by

$$(\nabla p)(\vec{x}_{i,j}) \approx \frac{(\pi_{i,j} - p_i)\vec{c}_{i,j}}{|\vec{c}_{i,j}|^2}. \quad (3.3)$$

Introducing the gradient evaluation in Equation 3.2 and regrouping terms yields

$$v_{i,j} \approx T_{i,j}(p_i - \pi_{i,j}), \quad T_{i,j} = A_{i,j} \frac{K_i \vec{c}_{i,j} \cdot \vec{n}_i}{\mu |\vec{c}_{i,j}|^2}, \quad (3.4)$$

where $T_{i,j}$ is referred to as the *one-sided* or *half-transmissibility* associated to the cell Ω_i and half-face $\Gamma_{i,j}$.

The *two-sided transmissibility* (or simply transmissibility) can be computed with some supplementary assumptions. Assume continuity of the pressure and flux across the half faces $\Gamma_{i,j}$ and $\Gamma_{j,i}$, meaning $\pi_{i,j} = \pi_{j,i} = \pi_{ij}$ and $v_{i,j} = -v_{j,i} = v_{ij}$. Then, express the pressure differential between the centre of the cell and the interface for both Ω_i and Ω_j as function of the flux across the cells using Equation 3.4, and subtract the two derived equations to eliminate the pressure at the interface π_{ij} and obtain the following

$$v_{ij} = T_{ij}(p_i - p_j), \quad T_{ij}^{-1} = T_{i,j}^{-1} + T_{j,i}^{-1}. \quad (3.5)$$

3.2 Medium definition and fine grid model

Since the focus of this thesis is the upward or vertical migration of CO₂, flow movement on the horizontal axis was disregarded and the studied porous medium, a vertical rock column modelled by a $1 \times 1 \times N$ grid where N is the amount of cell on the vertical axis. Additionally, it was assumed that there is no flow at the top and bottom of the column, preventing any form of leakage.

The physical parameters of the rock were defined as follow:

- Height of the rock column h : $h = 50$ m.
- Porosity of the rock ϕ : $\phi = 0.1$.
- The rock is considered incompressible.

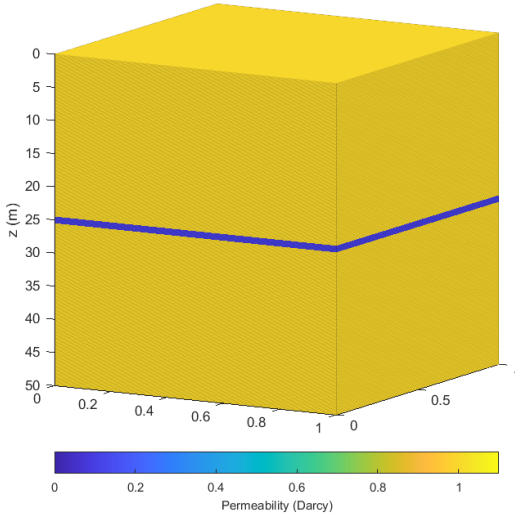


Figure 3.1: Permeability profile in the modelled rock column.

- Heterogeneous permeability was assumed along the vertical axis. A thin layer of lower permeability, also indistinctly called low-permeable layer, was placed in the reservoir at the middle of rock column while the permeability elsewhere in the reservoir was higher. The high permeability K_h was set to one darcy, i.e., $K_h = 1d \approx 9.87 \times 10^{-13} \text{ m}^2$. The low permeability K_l was given as a fraction of the high permeability and for this thesis, it was chosen that $K_l = K_h/10$.
- The thickness of the low-permeable layer was set to $e_l = 1 \text{ m}$. This value was chosen to illustrate the discrepancies in the vertical size between this low-permeable layer and the rest of the reservoir.

The terms of *lower* and *upper reservoir* are used to refer to parts of the reservoir respectively below and above the thin low-permeable layer. The surface at the top of the upper reservoir is referred to as *caprock*.

To simulate the flow behaviour in and around the lower permeability layer with a high degree of precision, we required that the grid modelling the media had at least 10 cells inside the low-permeable layer. For a grid of uniformed size cells, this required a grid with $N = 500$ cells. This grid is later referred to as the *fine grid*. Figure 3.1 depicts the medium's permeability field.

The properties of the fluids occupying the pore space are defined in Table 3.1

The last step was to define initial states. Numerical experiments were based on initial states where CO₂ was trapped under the water with a given distribution. The fluids were assumed immobile until the beginning of the simulations. A few examples of initial states

Table 3.1: Physical parameters of the fluids within the reservoir. cP [kg/m/s] (centiPoise), usual unit for dynamic viscosity. Corey-exponents are used to determine the relative permeability of the phase as described in Equation (2.16).

	Wettability	Density[kg/m ³]	Dynamic viscosity [cP]	Corey exponent
Water	Wetting phase	1014	1	2
CO ₂	Non-wetting phase	853	10	2

are displayed in Figure 3.2. Scenario 1, where half of the lower reservoir is filled with CO₂, prevailed in the experiments carried out. This means that simulations were run using this scenario if the initial state is not specified. Simulations were also conducted using other initial states to determine whether initial distribution of CO₂ had an impact on the results obtained and, if needed, quantify their effects.

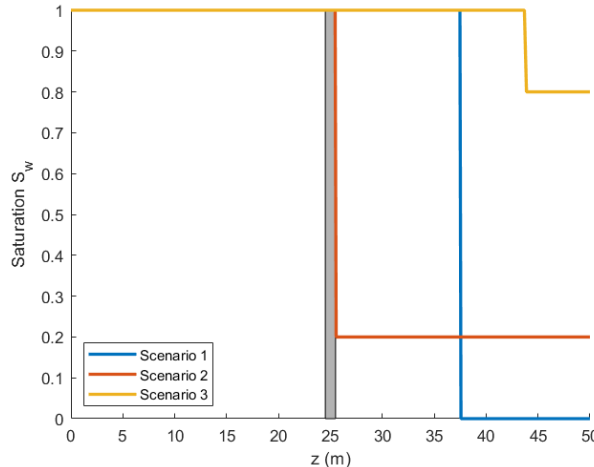


Figure 3.2: Examples of initial states used during numerical simulations. The horizontal axis on the graph denotes the depth given in meter and axis has reverse z -direction, with $z = 0$ m representing the top of the column and $z = 50$ m its bottom. The gray area at the centre of the column represents the low-permeable layer.

An initial simulation was run to observe and understand the flow behaviour that we want to reproduce when upscaling our model. Using Scenario 1 displayed in Figure 3.2, the flow behaviour of the multiphase fluid is given in Figure 3.3 for several times of simulation running t where t is given in years elapsed since the initial state.

The saturation profile depicted below and in subsequent graphs always refers to the brine saturation which we established as the saturation of reference in our model. The saturation profile of CO₂ can still be derived using Equation (2.10).

The first thing to notice is that despite its relatively low size, the thin layer of lower per-

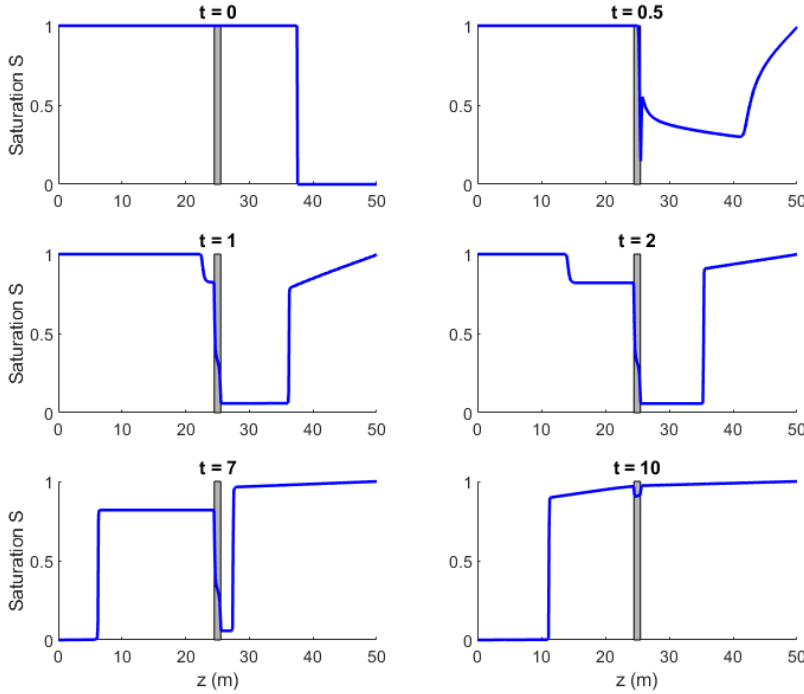


Figure 3.3: Snapshots of the fluid distribution evolution in the reservoir modelled by a fine grid starting from an initial state to an almost steady state $t = 10$ years later where CO_2 has essentially completed its upward migration. With 500 cells in the grid, Δx equals 0.1 m and 52 time iterations are run per year of simulations meaning that $\Delta t \approx 7$ days ≈ 1 week.

meability has a large impact on the flow behaviour. Thanks to our previous 1D analysis in the previous chapter, we know that the initial Riemann solution to the problem can be described based on Figure 2.8. Hence, from $z = 37.5$ m we have an upward moving shock with saturation below the shock equal to $S \approx 0.39$, a downward moving shock with saturation above the shock equal to $S \approx 0.29$, and a rarefaction wave linking the two shocks.

One can observe on the graph at $t = 0.5$ year that the saturation of CO_2 spikes to a large value below the thin layer (remember that we have $S_{\text{CO}_2} = 1 - S$). This happens when the shock formed at 37.5 m at initial time hits the low-permeable layer. Work from Section 2.4.3 indicates that the value of saturation below the layer will drop to approximately $S = 0.058$ and create a downward moving shock which will form an accumulation plume below the thin layer. At the bottom of the reservoir we observe an upward moving shock and a rarefaction wave spreading until the bottom of the reservoir and forming the plume's trailing edge. They were created after that the initial downward traveling shock wave collided with the bottom of the reservoir.

The graphs with $t = 1$ and $t = 2$ in Figure 3.3 depict a large-scale accumulation of CO₂ below the low-permeable layer. In the lower reservoir, we can easily distinguish a region of constant saturation with a discontinuity beneath it separating it from the rarefaction wave forming the tail of the saturation profile. The discontinuity is an upward traveling shock formed after the collision of the shocks described in the previous paragraph which ate away the rarefaction wave that separated them. This new shock will gradually slow down while approaching the thin layer and have an increasing brine saturation below (this evolution can be seen in the graphs for 1 year, 2 years and 7 years).

In the same two graphs we also see a decrease in the brine saturation above the thin layer. This decrease corresponds to the first significant quantities of CO₂ emerging from the low-permeable layer. It forms an upward moving shock from the low-permeable layer. On a more physical side of the world, we can say that this phenomenon occurred because a large portion of the CO₂ volume was still migrating upward while the first CO₂ molecules already hit the thin layer. Thus, the flow of CO₂ crossing the interface between the high-permeable layer and the low-permeable layer was not large enough to compensate the arrival of CO₂ in the newly formed accumulation plume below the thin layer. These graphs show that CO₂ slowly leaks through the thin layer. We can be more specific and add that the leakage of CO₂ migrating up in the upper reservoir formed a *plateau* with constant saturation or plume front.

After 7 years, the plume of CO₂ previously trapped under the layer has considerably shrunk and the lower reservoir is almost completely depleted of CO₂. The upward moving shock forming the bottom of the accumulation plume slowly approaches the low-permeable layer and when it will hit it, the constant CO₂ flow across the low-permeable layer will no longer be provided. At the top of the reservoir, the plateau of constant saturation has hit the caprock and created a downward moving shock where the saturation above the shock equals 0 corresponding to a pore space completely filled with CO₂.

In the last graph of Figure 3.3, the final and steady state is almost attained: quantities of CO₂ in the thin layer and below are minimal and the CO₂ forms a large plume at the top of the reservoir, accumulating against the caprock. In the upper reservoir, a downward traveling shock slowly increases the volume of the accumulation plume. Its velocity will slowly decrease and tend to 0 as time continues to increase.

This graphical analysis and qualitative flow behaviour explanation are valuable as they provide a good insight on what would happen if experiments based on these conditions were recreated in real life. They can also be used to determine which flow features we expect upscaled models to reproduce under simulations, such as the formation of an accumulation plume of CO₂ below the thin layer, the appearance of a plateau with constant height (i.e. saturation) on the upper side of the reservoir during the transfer of CO₂ between the two sub-reservoirs and more generally the formation, movements, and disappearance of shock waves and rarefaction waves.

The aim of later investigations is to decrease the resolution of the model by introducing *coarser grids*. Using these coarse grids for simulations would obviously lessen the achievable precision on the saturation profiles and therefore, expecting these profiles to represent detailed physical events such as shock waves appears as hopeless.

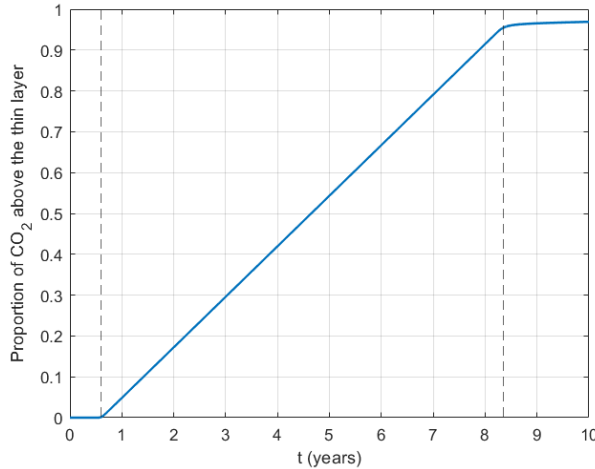


Figure 3.4: Evolution of the proportion of CO₂ that has reached the upper compartment after a given time t (with t in years).

Instead, we looked for other ways to establish whether a saturation profile evolution simulated on a coarse grid corresponded to a satisfying approximation of the original flow. Reservoir engineers are often more interested in general tendencies rather than detail evolution of the saturation within the reservoir. Thus, we defined a new useful tool that helped get a different look on the saturation evolution. The aforementioned tool consisted of computing the share of the initial quantity of CO₂ that had managed to reach the upper reservoir at a given time t . It is important to note that this indicator does not provide any information on how the CO₂ behaves within each compartment of the reservoir, solely describing how much CO₂ flowed from one sub-reservoir to the other. The evolution of this indicator, computed simultaneously during the simulation used for Figure 3.3, is displayed in Figure 3.4.

What stands out from this graph is its clear division into three stages.

At first, and as already observed in Figure 3.3, no flow of CO₂ is observed through the low permeable layer since the shock wave formed at the initial time and traveling upward is crossing the lower reservoir. When the shock wave of CO₂ reaches the low-permeable layer, it slowly permeates through the layer until the tip of the plume reaches the upper face of the thin layer while the tail of the plume is slowly accumulating beneath the layer. Until then, no significant quantities of CO₂ have reached the upper reservoir. This is represented in Figure 3.4 on the left-hand side of the graph by a constant share of CO₂ in the upper compartment equal to, or almost equal to, 0.

During the second phase, the graph shows a linear increase in the share of CO₂ indicating a constant rate of CO₂ permeating into the upper reservoir from the thin layer. This constant rate corresponds to the maximum in-flow the low-permeable layer can ingest from the accumulation of CO₂ below. This can be seen in Figure 3.3 after 2 years when a

plateau of constant saturation, led by an upward moving shock wave, emerges from the low-permeable layer. Since the upper reservoir can handle/receive a bigger flow than the thin layer, the low-permeable layer discharges all it can for as long as it is constantly fed from below, or equivalently for as long as the CO₂ accumulation plume below the thin layer is not depleted.

The last and third phase, on the right-hand side of Figure 3.4 occurs when the accumulation of CO₂ formed below the layer vanishes. More specifically, it happens when the shock wave at the bottom of the accumulation plume reaches the low-permeable layer. The constant flow is no longer provided to the low-permeable layer which in turn releases less CO₂ in the upper compartment: it simply depletes itself from any traces of CO₂. Hence the proportion of CO₂ increases but much slower than it did in the previous phase. The share of CO₂ will continue to grow slowly and approach 1 as time goes to infinity. What matters is that most of the CO₂ (approximately 95%) is stored in the upper reservoir and a large portion of the share is piled up against the caprock as another shock wave gently moves downwards, collecting the CO₂ as a plume resting below the caprock.

Thanks to these first experiments, a base knowledge about the characteristic features of the flow behaviour has been developed. It became more accessible to establish what up-scaled models should reproduce in terms of flow and potentially measure how well they perform in their approximation of this original flow. In particular, since the focus is to find coarse grid which mimic the flow transfer at the frontier, we evaluate their performance by comparing the share of CO₂ flowing into the upper reservoir.

Experiments

In this section, three upscaling techniques attempting to model the effects of the thin low-permeable layer on coarse grids have been implemented and tested. The first introductory method consists of defining the permeability field on coarse grids using the harmonic average. Building on the results from this first method, the second method aims to determine if there are appropriate permeability fields on coarse grids that generate flows similar to the flow generated by the fine grid permeability field. In addition, the second method aims to find a functional relationship between these coarse grid permeability fields and the rock's physical parameters. The last method is a variant of the second method where the transmissibility field, defined in Section 3.1.1, is the altered field rather than the permeability field.

4.1 Harmonic average of the permeability field

Contrary to other physical parameters like porosity, permeability does not have an additive property. Thus, computing the usual arithmetic average cannot be expected to return correct values for the permeability field. This implies that we need to find other ways to compute a permeability field defined on a coarser grid generating matching flow behaviour.

4.1.1 Experiment description

The absolute permeability K is an intrinsic property of the medium and therefore does not depend on the chemical species contained in pore space. Hence, equations derived for a single-phase flow, and more specifically Equation (2.8), are sufficient to get a first approximation of the upscaled absolute permeability. We denote the fluid potential by $\Phi = p - \rho g z$ and introduce it into Darcy's single-phase law, given in Equation (2.4) to get

$$\vec{v} = -\frac{K}{\mu} \nabla \Phi. \quad (4.1)$$

Inserting this into Equation (2.8) and scaling away the dynamic viscosity yields a Poisson equation with a variable coefficient.

$$\nabla \cdot (K \nabla \Phi) = 0. \quad (4.2)$$

Because Darcy's flow depends on the permeability K as shown in (4.1), one of the dominant approaches when upscaling K is to ensure that the upscaled permeability, denoted K^* , generates the same flow as the original permeability would. More specifically, because K^* is defined on a coarser grid, it is bound to be constant (homogeneous) on regions where K may not. Consider Ω , a cell of the coarse grid, and denote the upscaled permeability on this region by K_Ω^* . Then transcribing what was discussed means that we have

$$\int_{\Omega} K(\vec{x}) \nabla p \, d\vec{x} = \int_{\Omega} K_\Omega^*(\vec{x}) \nabla p \, d\vec{x} = K_\Omega^* \int_{\Omega} \nabla p \, d\vec{x}. \quad (4.3)$$

One of the most common ways to compute this upscaled permeability K^* is to look at the notion of power averages which is given by the following

$$K_\Omega^* = \left(\frac{1}{|\Omega|} \int_{\Omega} K(\vec{x})^p \, d\vec{x} \right)^{1/p}. \quad (4.4)$$

The harmonic average, computed from Equation 4.4 using $p = -1$, is of interest in our case considering that we focus on a 1-dimensional (1D) medium. It is indeed straightforward to show that the exact upscaled permeability in the 1D case is given by the harmonic average of the original permeability (see Lie, 2019, p.565).

Equation (4.4) can be reformulated to better express how the upscaled permeability K^* is computed for numerical simulations. Assume that Ω is a cell from the coarse grid on which the permeability is upscaled and $(\Omega_i)_{i \in I}$ the set of cells or piece of cells from the fine grid that are contained within Ω , in other words $\Omega = \cup_{i \in I} \Omega_i$. Let K_i be the permeability associated to the cell with Ω_i with volume $|\Omega_i|$. Then, performing the harmonic average of the permeability on Ω reads

$$K_\Omega^* = \frac{|\Omega|}{\sum_{i \in I} \left(\frac{|\Omega_i|}{K_i} \right)}. \quad (4.5)$$

4.1.2 Results

To compare the flow obtained for upscaled permeability and the original flow behaviour, several coarse grids were defined. These coarse grids had a lower resolution than the fine grid had (a scale reduction of at least ten), an identical porosity and a permeability field determined by the harmonic averaging the permeability of the fine grid as described in Equation (4.5). A first overview of the computed permeabilities is given in Figure 4.1. We note that the thin low-permeable layer from the fine grid slowly becomes thicker and has higher permeability as the resolution of the grid decreases.

It can be tempting to believe that a thicker layer with slightly higher permeability has the same effect on the flow than a thin low-permeability layer but simulations ran on the

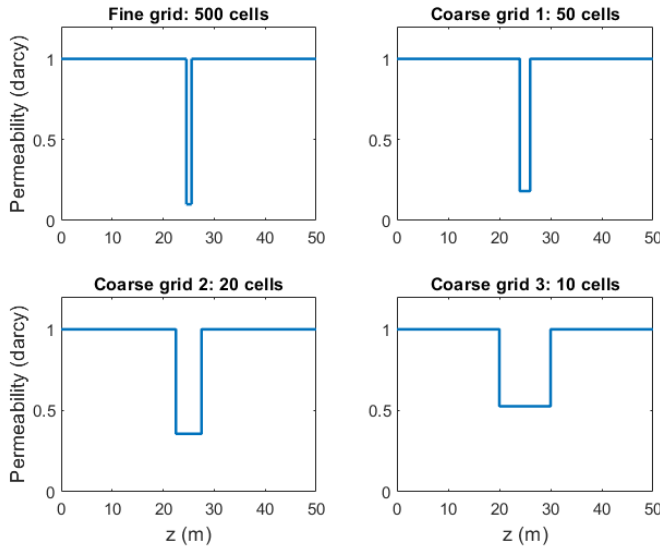


Figure 4.1: Permeability (in darcy) within the reservoir as originally defined for the fine grid and computed via the harmonic average for three coarse grids.

columns described previously indicate otherwise. Figure 4.2 depicts the computed saturation profiles after respectively 1 year, 4 years, and 10 years.

As claimed at the end of Section 3.2, Figure 4.2 illustrates how unlikely it is that simulations on coarse grids yield saturation profiles with shock waves or similar phenomena as they are smoothed out. This is more apparent the coarser the grid is. For instance, the grids with 20 and 10 cells can make it challenging to determine if there are actually shock waves in the saturation profile without comparing them with the fine grid saturation profile.

Figure 4.2a shows the evolution after 1 year and illustrates that the flow features obtained for the fine grid do not match those of the coarse grids. The simulation on the 10-cell grid shows that too much CO₂ leaks in the upper reservoir and that the accumulation of CO₂ beneath the thin layer is not as significant as expected. In the case of the 50-cell grid and 20-cell grid, the saturation fits a bit better the general expected shape and it has some similar characteristics with the fine grid saturation even though there are noticeable hints that they still let too much CO₂ flow through the low-permeable layer.

Figure 4.2b shows that none of the coarse grid-based simulations approximate correctly the fine grid flow features. Indeed, the first significant quantities of CO₂ are barely reaching the caprock of the column after 4 years for the fine grid while it already started to accumulate at the top for every coarse grids. Furthermore, the accumulation plume below the layer has vanished for every grid but the fine grid, highlighting even more that the harmonic average based method lets too much CO₂ flow through the thin layer.

The saturation profiles after 10 years, as displayed in Figure 4.2c, are fairly similar but this

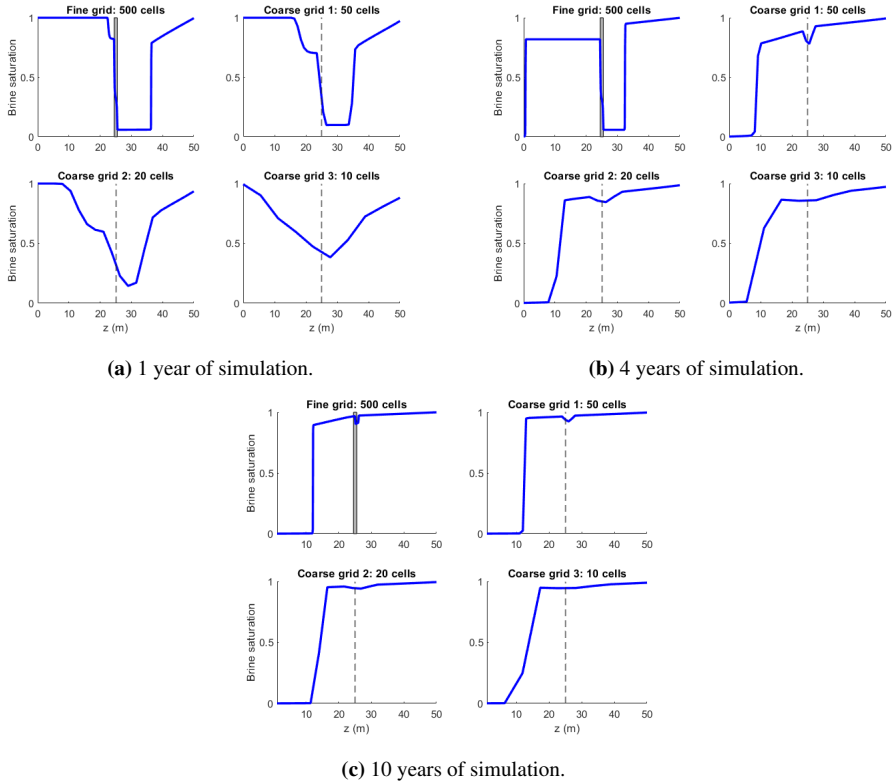


Figure 4.2: Comparison of the saturation profile evolution after 1, 4, and 10 years. The coarse grid permeability fields are computed by harmonic averaging the fine grid permeability field.

is expected. Simulations have almost reached the final and steady state corresponding to the nearly complete accumulation of CO₂ near the caprock which is identical for all grids.

The first overall impression left by these simulations was that permeabilities upscaled by harmonic averaging generated permeability fields on coarse grids that let too much CO₂ flow upward and had a lower permeability value that was too high. This is confirmed by looking at the evolution of the share of CO₂ in the upper reservoir in Figure 4.3.

Figure 4.3 emphasises that none of the coarse grids have been able to approximate the correct flow of CO₂ from the lower to the upper reservoir. In particular the coarse grid 1 (50 cells) and coarse grid 2 (20 cells) were said to have flow behaviour partially approximating the fine grid's flow after the first year of simulation. Yet, they had respectively three times more and six times more CO₂ in their upper reservoir than their fine grid counterpart at that time. This illustrates further that the harmonic averaging method is unable to mimic the specific features of the original flow and more specifically it is apparent once again that the plume of CO₂ permeates through the low-permeable layer too quickly.

Graphs displayed above were obtained for simulations based on coarse grids with an even

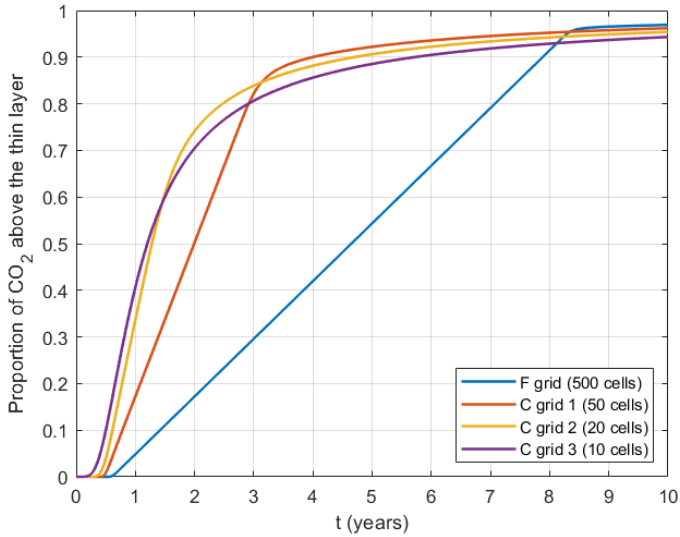


Figure 4.3: Proportion of the initial quantity of CO_2 accumulated in the upper part of the reservoir, i.e. that has flowed through the zone of lower permeability, as a function of time t (given in years).

number of cells, but the general impressions and conclusions remain identical for coarse grids with an odd number of cells (i.e., a 49-cells grid yields similar result than a 50-cells grid). However, it is worth noting that there is a notable distinction between these two cases.

The reservoir was defined with a certain symmetry (the low-permeable layer sits precisely at the centre of the column) and harmonic averaging the fine grid permeability field preserves this symmetry. Therefore, a coarse grid with an even number of cells has two cells with lower permeability (when the number of cells is low enough). On the other hand, only a single cell has its permeability affected if the grid has an odd number of cells (again, when the total number of cell is low enough).

Let n_c denote the number of cells in a coarse grid. If n_c is even, then the thickness of the low-permeable layer in the permeability field generated on the coarse grid equals $2h/n_c$. If n_c is odd, this thickness equals h/n_c . This implies that the low-permeable layer's thickness is almost twice as big for coarse grids with an even number of cells when compared to coarse grids that have similar, yet odd, number of cells.

This leads to very awkward model representation for coarse grid based on small even number of cells where the size of the layer becomes much bigger than the size of the original low permeability layer. This is illustrated in Figure 4.4 where the low-permeable layer ends-up representing 20% of the column or equivalently 10 m from the initial 50 m.

Besides generating coarse grids with much thicker lower permeability layer as described in Figure 4.4, harmonic average's definition also induces that the lower permeability in

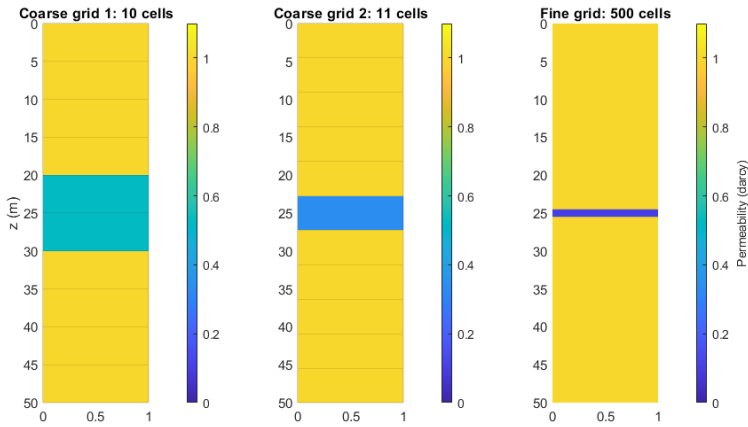


Figure 4.4: Size comparison of the low-permeability layers between two coarse grids on the left and middle, respectively 10 and 11 cells, and the initial fine grid with 500 cells.

the coarse grid's permeability field gradually increases when reducing the amount of cell in the model. This means that the low permeability K_l is progressively diluted into these larger cells, preventing the newly defined model to accurately represent the existence of an altered and slowed flow at the centre of the reservoir.

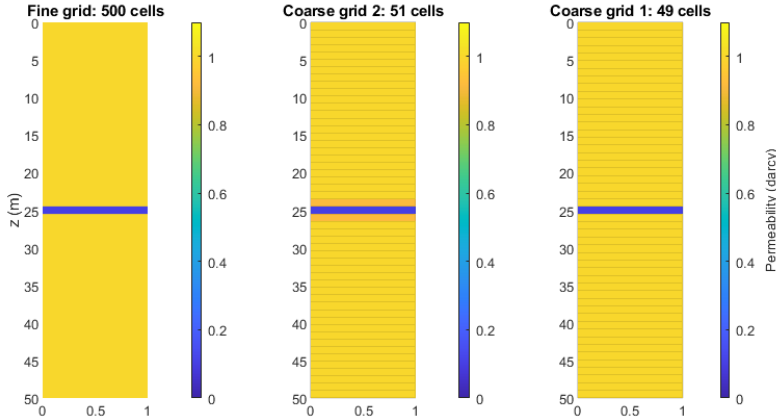
It is also interesting to point out that even coarse grids whose permeability fields approximate rather accurately the original physical problem, as seen in Figure 4.5a, still generate flow which suffer a lack of accuracy. Indeed, simulations on coarse grids with 49 and 51 cells resulted in a completely different evolution of the share of CO₂ in the upper reservoir than the one on the fine grid as depicted in Figure 4.5b.

Thus, Figure 4.5 illustrates that it is not sufficient to have a permeability field that *looks alike* the one from the fine grid to derive a flow behaviour similar to the one expected.

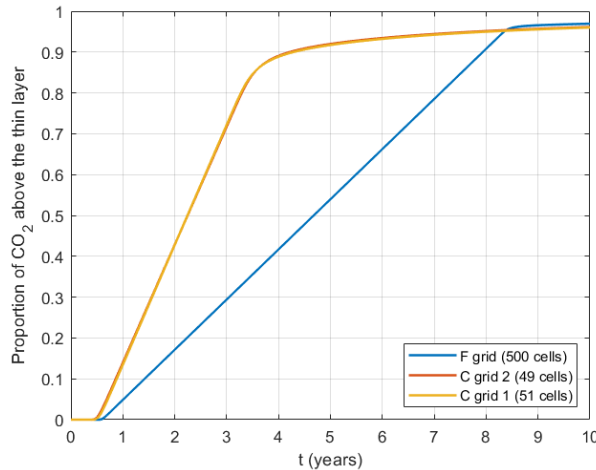
4.1.3 Overview and discussion

The overall conclusion that was drawn out of this series of simulations was that performing a harmonic average of the permeability field from the fine onto coarse grids resulted in flow behaviour that were nowhere near similar to the flow behaviour simulated on the fine grid, which the flow that we wanted to match. Whether the grid was defined with an even or an odd number of cells, whether the computed permeability fields induced a physical model that was fairly similar to the original physical model or a completely different one, or whether the simulations were run on a coarse or highly coarse grid, none of these models or grids were able to generate appropriate flow that would be similar to the one obtained for the fine grid.

Although potential explanations to these poor approximations have been discussed along this section, they are most likely underlying consequences of the fact that this upscaling is



(a) Permeability field for a fine grid with 500 cells and two coarse grids with respectively 51 and 49 cells.



(b) Evolution of the share of CO_2 in the upper compartment for all three grids defined above. Note that the curve obtained for the coarse grids are almost indistinguishable.

Figure 4.5: Comparison of three grids, the fine grid and two coarse grids, representing a similar underlying physical model where the low-permeable layer has approximately the same thickness and permeability value. Despite this resemblance, the flow behaviour in the coarse grids is far different from the one obtained for the fine grid.

based on single-phase flow as described in Equation (4.2) which inevitably hits its limits when considering a two-phase flow.

This section has showed that the harmonic average could not provide permeability fields on coarse grids resulting in a flow behaviour similar to the one generated by the fine grid. Therefore, an alternative method based on the similar concept of altering coarse grids' permeability field was investigated.

4.2 Functional relationship for the permeability field

Among the issues raised at the end of previous section, it was emphasised that the permeability fields for the coarse grids derived using the harmonic average were too permeable in the thin layer region, inducing a faster upward CO₂ migration than the one wished for.

4.2.1 Experiment description

Along this subsection, we describe the second method implemented where we attempted to derive a functional relationship between the permeability field on coarse grids and the rock's geophysical parameter. The search for this functional relationship relied on extrapolating patterns observed in experiments carried out.

Specifically, the objective here was to determine whether there existed ideal or optimal permeability fields that generate flow of CO₂ matching the expected flow computed on the fine grid. If such permeability fields existed, we looked for ways to compute them based on the physical quantities of the grids only. We denote the lower permeability in the coarse grids by K_{lc} , the thickness of the low-permeable layer and high-permeable compartment in the fine grid respectively by e_l and e_h , and the thickness of the low-permeable region in the coarse grid e_{lc} . We look for an expression of K_{lc} as a function of K_l , K_h , e_l , e_h and e_{lc} :

$$K_{lc} = K_{lc}(K_l, K_h, e_l, e_h, e_{lc}). \quad (4.6)$$

4.2.2 Results

High permeability K_h

In Equation (4.6), we stated that K_{lc} may depend on the high permeability of the fine grid. However, it seemed more rational that changes in the high permeability in the fine grid K_h would require changing the high permeability of the coarse grid K_{hc} rather than the lower one K_{lc} . Thus, it was further assumed K_{lc} did not depend on K_h . Hence, we take this into account in Equation (4.6) to get

$$K_{lc} = K_{lc}(K_l, e_l, e_h, e_{lc}). \quad (4.7)$$

Finding an initial value for K_{lc}

Given that the existence of such permeability fields is not guaranteed, we started by simulating the flow evolution of the CO₂ in different coarse grids with altered permeability

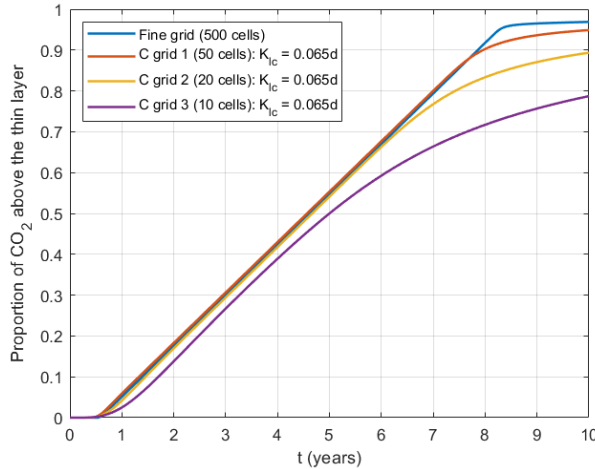


Figure 4.6: Proportion of the initial quantity of CO_2 that reached the upper reservoir as a function of time (given in years).

K_{lc} at the centre of the model to reflect the original physical problem. What arose from these simulations was that it was possible to find permeability fields that helped to partially reach the expected flow behaviour, as depicted in Figure 4.6.

Finding a good permeability field relied on an extensive search through the repetition of simulations and feedback loops. We started with a given permeability field: we fixed $K_{hc} = K_h$ and $K_{lc} = K_l$. Then, the flow was simulated for coarse grids with permeability field as defined and it was compared with the expected flow generated on the coarse grid. To determine if a permeability field generated the correct flow, the quantity of CO_2 flowing into the upper reservoir and its flow rate were compared between the fine and coarse grids. If CO_2 leaked upward too quickly, the lower permeability in the coarse grid K_{lc} was decreased to simulate a more impermeable layer. If the fluid connection between the two reservoirs was too weak, the lower permeability K_{lc} was increased. These steps were repeated until they generated a similar flow rate at the interface during the ramp-up phase. Figure 3.4 depicts the flow of CO_2 across the low-permeable layer on the fine grid and 3 coarse grids with respectively 50, 20, and 10 cells where the permeability fields of the coarse grids have undergone the process described above. When the resolution was sufficiently high, we also relied on the comparison of the saturation profile to check whether specific flow features were correctly represented on coarse grid-based models. However, this last idea was of limited use for coarse grid since they tend to average out any local phenomenon that can occur.

Although this approach was based on a simulation loop to determine the permeability field, which is definitely something to avoid for a full-scale model, it aimed to obtain a predictive and generalised way to determine the optimal permeability field for a given coarse grid.

In the end, the lower permeability K_{lc} was found to be equal to 0.065 d for grids with even

number of cells and equal to 0.038 d for grids with an odd number of cells. In Figure 4.6, the displayed simulations have been run on three coarse grids with lower permeability given by $K_{lc} = 0.065$ d. Looking at the graph, we see that the selected suitable permeability fields generated accurate approximations of the CO₂ flow rate between the two reservoirs for several years: 7.5 years for the 50-cell grid and up to 6.5 years for the 20-cell grid. The 10-cell grid generates a fairly similar flow to the rest of the grids for early years with an offset. This offset can be explained by the thickness of the low permeable layer at this point: for a 10 cell-grid, the low permeable layer represents 2 cells of the grid, or equivalently 20%, meaning it takes 10 m of the total column.

However, no matter the number of cells in the coarse grids, we also observe that the tails of the curves are noticeably different after the ramp-up phase. More specifically, the upward migration of CO₂ in coarse grids seems to be much slower when approaching the steady state. For example, it takes about 7.5 years for 70% of the CO₂ share to leak into the upper reservoir for the 10-cell coarse grid while the fine grid's upper reservoir has already collected 85% of the total CO₂ share by then, exceeding the 70% threshold over a year earlier. This implies there is a period of time during the simulation where these optimal permeability fields do not provide a flow behaviour that is reliable and similar to the one obtained for the fine grid.

This search for optimal permeability fields also highlighted once again the difference between the coarse grids with an odd or even number of cells. We let n_c denote the number of cells in a coarse grid. For grids where n_c is odd, the lower permeability value K_{lc} was lower than the one obtained for even-numbered cell grids. In particular, when n_c was odd, we obtained that $K_{lc} \approx 0.038$ d while we found that $K_{lc} \approx 0.065$ d for the grids where n_c was even. This difference can be explained yet again by the fact that even-numbered cell grids have two cells with low permeability, meaning it is possible to *relax* the permeability value constraint a bit. Odd-numbered cell grids only have a single cell with lower permeability which requires the flow to be strongly slowed down when flowing through this single cell.

Additionally, we note that simulations on grids with an even number of cells yielded slightly better approximations of the flow overall. To quantify this difference, we defined an error function which is expressed as the square of the difference between the quantity of CO₂ in the upper reservoir at a given time for the fine grid and the same quantity of CO₂ computed on the coarse grid. For example, the error curve for the grid with 20 cells in Figure 4.7a (yellow curve) is obtained by squaring the difference between the fine grid curve in Figure 4.6 (blue curve) and the 20-cell grid curve on the same graph (yellow curve).

Figure 4.7 displays the error for 3 grids with an even number of cells (the same grids that were used in Figure 4.6) and 3 grids with an odd number of cells. We can see that the error for grids with an odd number of cells is about twice as large at any time than the error for even-numbered cell grids for a similar number of cells in the grid.

The existence of suitable permeability fields for our initial model set-up was encouraging and therefore, we continued to investigate the impacts that the parameters had on the choice of the low permeability value as described in Equation (4.7).

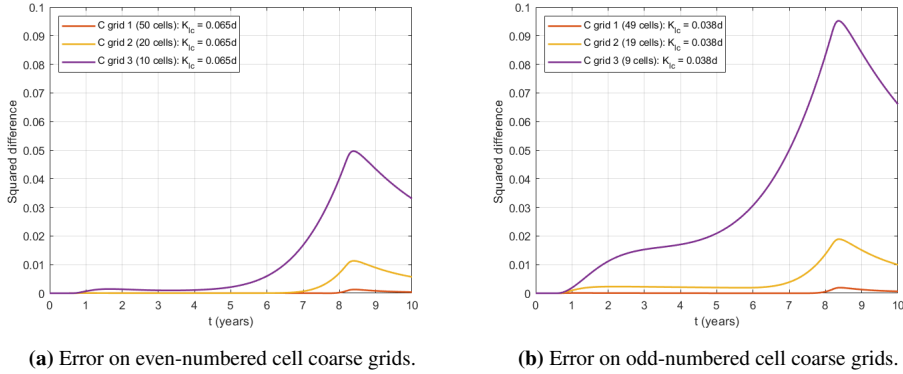


Figure 4.7: Measure of the quality of the approximation realised by simulations ran on coarse grids. The error measure is based on the squared difference between the expected quantity of CO₂ in the upper reservoir at a given time and the computed one, i.e. the quadratic error. Here, it illustrates that the error for coarse grid with an odd number of cells is twice as large.

Thickness of the coarse grid's low-permeable layer e_{lc}

From Figure 4.6 and supplementary simulations, we also noted that the coarse grid resolution did not seem to have an impact on the choice of the value for the lower permeability when the parity of the number of cells in the grid is maintained while decreasing the resolution. Indeed, we see that the 50-cell grid, the 20-cell grid, and the 10-cell grid all required to have a permeability field where the lower permeability was given as $K_{lc} = 0.065$ d. Likewise, the choice for K_{lc} for grids with an odd number of cells was identical for all odd values of n_c as well, with $K_{lc} = 0.038$ d.

To summarise, n_c does impact the appropriate choice of K_{lc} but only through its parity. The thickness of the low-permeable layer in coarse grids is $e_{lc} = 2h/n_c$ if n_c is even and $e_{lc} = h/n_c$ if n_c is odd. This means that a 50-cell grid and a 25-cell grid both have the same thickness for their low-permeability layer. Yet, they have distinct lower permeability values. Furthermore, we saw earlier that grids with 10, 20 and 50 cells (and more generally grids with an even number of cells) all generated an ideal flow for the same value of K_{lc} while the thicknesses of their low-permeable region are different.

Hence e_{lc} does not impact K_{lc} . However, to take into account that the parity of n_c influences K_{lc} , we define $C(n_c)$ a dimensionless function which only has two outputs depending on the parity of n_c .

We rewrite Equation (4.7) as

$$K_{lc} = F(K_l, e_l, e_h) \times C(n_c). \quad (4.8)$$

Thanks to Figure 4.7, we know that coarse grids with an even number of cells yield better approximation of the flow rate at the frontier. Therefore, the focus will be placed on coarse grids with an even number of cells for the remainder of this section.

Influence of the low permeability K_l

So far, we had only used a lower permeability value of a tenth of the larger one, $K_l = 0.1 \times K_h$. Additional fine grids were created where the permeability in the layer was still smaller than the higher one K_h but varied a bit.

A good understanding of the physical model hinted at the fact that the correct low permeability for a coarse grid K_{lc} was potentially proportional to the low permeability K_l in the thin layer. This hypothesis was motivated by the will to find coarse grid permeability fields that correctly reproduce the flow of CO₂ between the reservoirs during the ramp-up phase. This means that we expected the permeability fields to generate flows similar to the fine grid's flow, and such flows are connected to the Darcy's flux velocities which themselves are proportional to the absolute permeability as shown in Equation (2.20).

In order to test this conjecture, we defined new fine grids with slightly altered permeability value in their thin layer. In particular, these new low permeability values were given as γK_l , where γ was the coefficient denoting the change in permeability in the thin layer. For our set of fine grids defined and used in simulations illustrated in Figure 4.8, γ took its values from {0.1, 0.5, 1.5, 2}.

Then and for each fine grid, we defined their respective coarse grids and their associated permeability field. According to our hypothesis, a coarse grid aiming to mimic the flow of a fine grid with low permeability of γK_l would have its lower permeability set to γK_{lc} .

For instance, the permeability field of the coarse grid with 50 cells had a low permeability given by $K_{lc} = 0.065$ d when the permeability in the original fine grid was given by $K_l = 0.1$ d. In a new fine grid where instead the permeability in the thin layer would be given by $K_{l\gamma} = \gamma \times K_l$, the lower permeability value in the coarse grid of 50 cells was predicted to be given by $K_{lc\gamma} = \gamma \times K_{lc}$.

After building the models as defined above, we simulated their evolution in time. Figure 4.8 is the compilation of the time evolution of the CO₂ proportion that has reached the upper compartment for 4 fine grids, each defined with a distinct lower permeability, and their associated coarse grids.

Considering that the curves generated on coarse grids and displayed in Figure 4.8 were based on predicted permeability fields, they do result in particularly good approximations of the CO₂ flow into the upper reservoir. For every fine grid, the curves obtained for coarse grids provide accurate estimation of the CO₂ migration for a large chunk of the simulation, specifically during the ramp-up phase. The limits of the method are still apparent for lower resolution grids which generate lower exchanges of CO₂ between the compartments much earlier than the fine grid simulations do.

Also note that the time scale on each graphs of Figure 4.8 has been adapted to see most of the CO₂ migration. We notice that the corresponding time scale necessary to attain or approach the steady state phase is roughly inversely proportional to K_l . Indeed, the fluids can move more easily in the high permeability compartments of the reservoir. Hence, the time scale at which most of the CO₂ will reach the upper reservoir depends on its ability to permeate the thin layer. The lower K_l is, the harder it is for the CO₂ plume to permeate

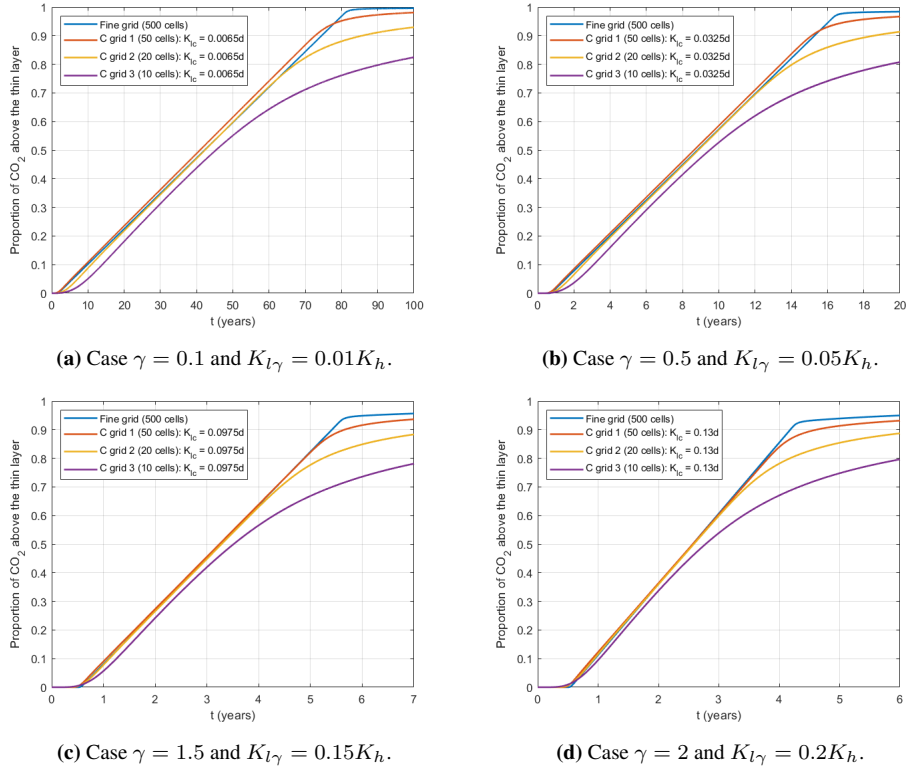


Figure 4.8: Time evolution of the share of CO_2 leaking into the upper reservoir for different low permeability values in the thin layer in the fine grid and predictive permeability values in the coarse grids. These 4 graphs illustrate the existing proportionality between the permeability in the thin layer from the fine grid and the low permeability needed on coarse grids to match the flow behaviour.

through the thin layer and thus the longer it takes to reach the third stage.

These new findings provided us with a better formulation of Equation (4.8) which reads

$$K_{lc} = K_l \times C(n_c) \times G(e_l, e_h) = K_l \times C(n_c) \times \tilde{G}\left(\frac{e_l}{e_h}\right), \quad (4.9)$$

with G and \tilde{G} dimensionless functions depending on e_l and e_h . The second equality of Equation (4.9) is motivated by the fact that we look to multiply the permeability K_l with a dimensionless parameter so that we end up with K_{lc} , which is also a permeability. The only way to produce a dimensionless parameter from a function G depending e_l and e_h is to consider another function \tilde{G} which depends on the ratio of the two thicknesses.

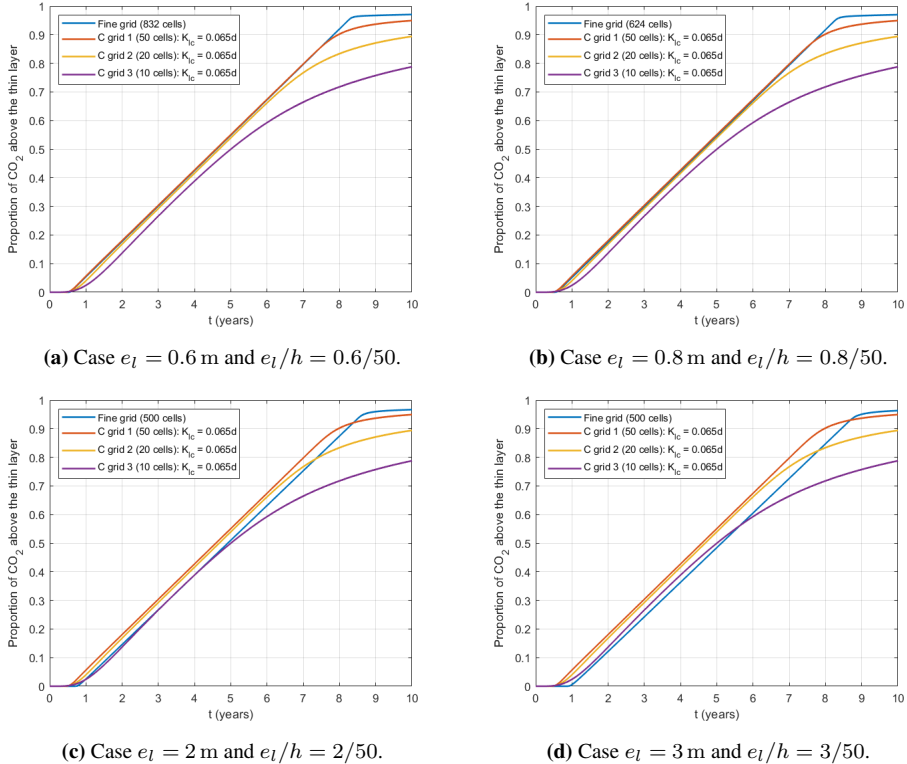


Figure 4.9: Time evolution of the share of CO₂ leaking into the upper reservoir for different low-permeable layer thickness e_l . The 4 graphs presented illustrate that the thickness merely impact the flow rate by the introduction of an offset.

Height of the reservoir h and low-permeable layer's thickness e_l

Therefore, the last step consisted of investigations determining the effect of modifications of the ratio e_l/e_h on the choice of an acceptable permeability field for a given coarse grid.

We note that $h = 2e_h + e_l$ and thus an other way to look at the ratio e_l/e_h was to consider the ratio e_l/h which may be more intuitive to visualise. Up until now the initial ratio used for all simulations had been $e_l/h = 1/50$ and we proceeded to simulate the flow behaviour for other values of the ratio, as shown in Figure 4.9. The column remained defined with constant height of $h = 50$ m and only the thickness of the low-permeable layer was altered.

The graph illustrates that changes on the ratio e_l/h did not impact the rate of CO₂ flowing into the upper compartment during the ramp-up phase but rather created an offset in the proportion profile. For instance, it delayed the arrival of the first visible quantities of CO₂ in the upper reservoir for thicker low-permeable layers which was expected since the flow was slowed down for a larger portion of the reservoir. This meant that although

the proportion of CO₂ may be different at a given time for two fine grids with different thicknesses of the low-permeable layer, the permeability field best suited to model their flow behaviour would be the same since it aimed to reproduce the same rate of CO₂ flowing from one compartment to the other.

Hence, taking this into account, we modified Equation (4.9) one last time to get

$$K_{lc} = C(n_c) \times K_l, \quad (4.10)$$

where $C(n_c)$ is dimensionless constant. Based on previous simulations, we had $C(n_c) = 0.65$ for coarse grids with an even number of cells and $C(n_c) = 0.38$ for odd-numbered cell grids.

Impact of the initial state

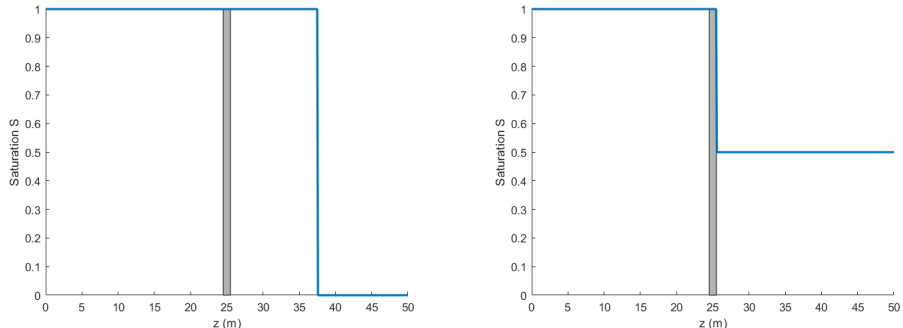
Thus far, the impact of initial states had been overlooked to focus on effects of intrinsic physical parameters of the grids. The only initial state used for simulations in this subsection up until now had been the scenario depicted in Figure 3.2 as Scenario 1, where the lower half of the bottom reservoir in completely filled with CO₂. We now conclude this section with an investigation of the effects of the initial state on the flow approximations generated by permeability fields generated according to Equation (4.10).

There are countless ways to define an initial state. Hence, the first part of the work done here was to determine which simulations had to be compared with another. With a bit of work, it became apparent that the initial state's characteristic truly impacting the flow behaviour through the low-permeable layer was the quantity of CO₂ initially stored in the lower reservoir rather than the precise distribution of CO₂ within this compartment. Before attempting to explain why this would occur, we provide the reader with an example.

Simulations were run on coarse grids with their associated permeability field defined according to Equation (4.10). Figure 4.10 compares the leakage of CO₂ between the lower and upper reservoir for two different initial states. The first one is the one used for simulations consistently along this section and named Scenario 1. These two initial states were defined to have the same quantity of CO₂ stored in their lower reservoir at initial time but have a different initial saturation profile as illustrated in Figures 4.10a and 4.10b.

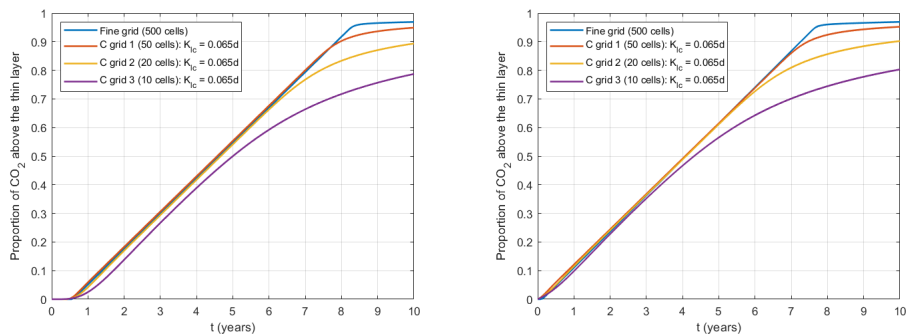
Despite this difference of CO₂ distribution at initial time, the curves depicting the exchanges of CO₂ between the two sub-reservoirs, given in Figures 4.10c and 4.10d look practically identical for grids with the same number of cells. There are minor perturbations or differences but the shape of the curves seems to be preserved. In particular, despite a change in the initial state, the approximation of the fine grid flow behaviour still holds for the same permeability field as defined by Equation (4.10). One noticeable change is the disappearance of the offset in the 10 grid cells curve in Figure 4.10d. This disappearance can be explained by the fact that CO₂ is already at the frontier when the simulation starts rather than having to first migrate upward before hitting the low-permeable layer.

This first simulation pointed to the fact that for initial states that differ in their fluid distribution but are comparable in the quantity of CO₂ introduced in the system, the permeability field generating good approximations of the flow behaviour of the fine grid was identical.



(a) Initial state corresponding to the scenario 1, which has been used for simulations in this section so far.

(b) Initial state where the whole lower reservoir is partially filled with CO_2 .



(c) Share of CO_2 as obtained for the initial state given above, known as scenario 1.

(d) Share of CO_2 as obtained for the initial state given above.

Figure 4.10: Saturation profiles at initial time and their associated graphs depicting the leakage of CO_2 into the upper compartment. The two initial states were defined to fill half of the lower reservoir with CO_2 but with a different distribution within the compartment.

This flow behaviour similarity can be explained by remembering that the presence of a low-permeable layer in the reservoir creates a situation in which CO_2 's upward migration is significantly slowed. This then leads to an accumulation of CO_2 below the thin layer as described in Figure 3.3. This means that the time frame in which CO_2 crosses the lower reservoir is much shorter than the one describing its leakage through the low-permeable rock. Hence and because of this time frame difference, two initial states with comparable quantity of CO_2 distributed differently will generate a similar evolution of the accumulation plume below the thin layer, although it may form a bit sooner or later depending on the original distribution. Given that these initial states produce a comparable accumulation of CO_2 below the low-permeable layer, the ramp-up phase and the depletion phase described in Figure 3.4 will be similar too and this explains why Figures 4.10c and 4.10d share a lot of common characteristics.

This initial observation was further endorsed with the help of supplementary simulations

based on diverse initial states. To emphasise the influence of the initial quantity CO₂ on the results, Figure 4.11 regroups three simulations based on different initial states that all induced a quantity CO₂ representing a quarter of the lower reservoir's volume.

Here again we see that, on grids of the same size, different initial states yield evolution of CO₂ leakage into the upper reservoir that are fairly similar (except for a small offset) for rocks defined with an identical permeability field despite large variations in the original phase distribution.

However, and contrary to the simulations in Figure 4.10, the flow behaviour obtained for low resolution grids does not resemble the fine grid's flow behaviour for the permeability field as defined previously. To be more specific, the flow behaviour obtained for a 50-cell grid still matches the fine grid's flow. The flow generated for a 20-cell grid has similar flow rate through the frontier (slightly decreased) and is delayed when compared to the fine grid flow. The flow generated on coarser grids (e.g., a grid with 10 cells) indicates that the permeability field used earlier excessively slows down the flow of CO₂ through the low permeable layer.

It follows that defining permeability fields on coarse grids solely based on rock's physical parameters is inaccurate in the general case, especially when looking at grids with a very low resolution.

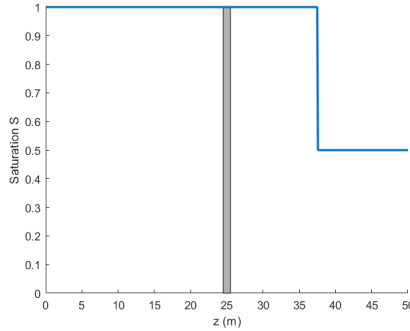
4.2.3 Overview and discussion

Along this section, we first assumed the existence of a functional relationship between the lower permeability in a coarse grid and the geophysical parameters of the medium and investigated which parameters would actually influence it and how. We ended-up with a rather simple relationship given in Equation (4.10) where the only physical parameter affecting the choice of K_{lc} was the lower permeability from the fine grid K_l .

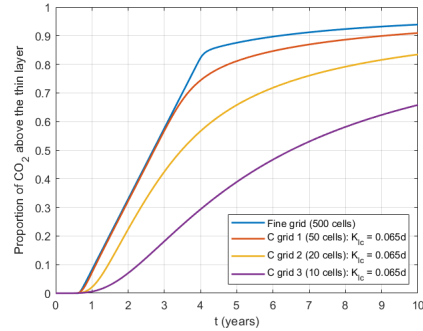
Strictly speaking, we also observed that K_{lc} depended on n_c , the number of elements in the coarse grid, and more specifically on its parity, a non-physical parameter of the reservoir. Nevertheless, this dependence to a non-physical parameter can be explained and handled by differentiating the case of grids with an odd or even which induce a different symmetry problem. Hence for a given parity of n_c , this dependence is only modelled by a coefficient constant. We also note that, similarly to the harmonic averaging method, the low-permeable layer for coarse grid has an increasing thickness when the resolution decreases which then can then lead to a poor representation of the original physical problem.

Additionally, after deriving a reasonable expression for the functional relationship determining permeability fields on coarse grids and generating the same flow rate through the low permeable layer, we tested the method's validity and robustness against changes in the initial state. The quality of the flow approximation was shown to depend on the initial state and more specifically on the quantity of CO₂ trapped under the thin low-permeable layer: although the method did provide a notable level of accuracy in the approximation when the quantity of CO₂ was important, we observed that there was no proper approximation of the flow in the general case.

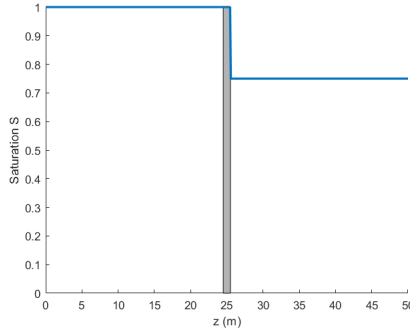
This dependence implies that the hypothesis stated at the beginning of the section where



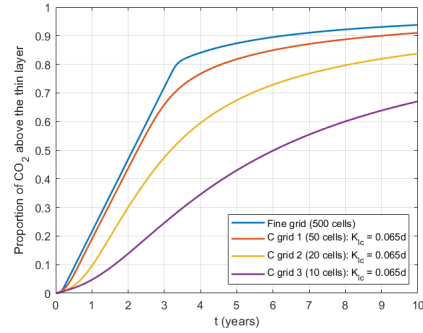
(a) Initial state where the lower half of the bottom reservoir is partially filled with CO_2 .



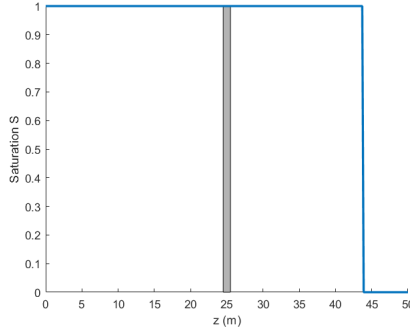
(b) Time evolution of the CO_2 proportion reaching the upper reservoir starting from the initial state on the left.



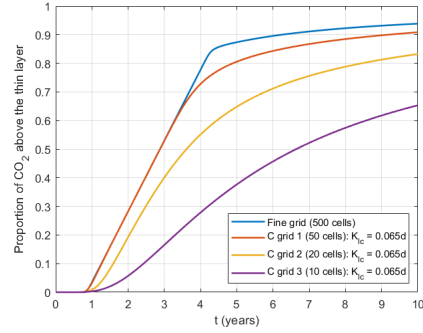
(c) Initial state where the whole bottom reservoir is partially filled with CO_2 .



(d) Time evolution of the CO_2 proportion reaching the upper reservoir starting from the initial state on the left.



(e) Initial state where the lower quarter of the bottom reservoir is completely filled with CO_2 .



(f) Time evolution of the CO_2 proportion reaching the upper reservoir starting from the initial state on the left.

Figure 4.11: Initial states and their associated evolution of the proportion of CO_2 leaking into the upper compartment for three initial states where the distribution is different but all correspond to situations where a quarter of the lower reservoir is filled with CO_2 .

we assumed the existence of a functional relationship depending on physical parameters only is erroneous. To obtain flow approximations that consistently matching the fine grid flow behaviour, a dependency on the saturation would need to be included. This completely contradicts the hopes built for this method. However, we can nuance this by pointing out that the method still provides flow rate approximations that do match the fine grid flow rate under specific conditions: a constant flow rate into the low-permeable layer which happens for a well-established plume of CO₂.

4.3 Changes in the transmissibility

One of the issues raised throughout the previous section was that a large decrease in the vertical resolution yields coarse grids whose cells are much thicker than originally. Hence, altering the permeability field on these coarse grids creates a mismatch between the original physical model and the ones created with coarse grids. Thus, an alternative approach was investigated.

4.3.1 Experiment description

Rather than attempting to modify the permeability fields, the last method considered had for purpose to alter the transmissibility field. Numerically, permeability fields are defined as constant within the cells, while transmissibility fields have the convenient property to be defined on the faces of each cells rather than on the cells as a whole, as detailed in Section 3.1.1.

Similarly to what had been done for permeability fields on coarse grids, we wanted to find out whether there existed transmissibility fields on coarse grids which could generate a flow similar to the one obtained on the fine grid and how the different physical parameters of the rock would influence it.

In grids defined with an even number of cells, the middle of the column sits precisely at the interface of two cells. Considering the large discrepancies in size between the low-permeable layer and the rest of the reservoir, it can be appropriate to reduce the layer to an interface blocking or slowing down flow passing through it. Hence, on even-numbered coarse grids the impact of the thin layer can be modelled as a reduction of the transmissibility at the centre of the reservoir. For coarse grids with an odd number of cells, the centre of the reservoir sits within the *middle cell*. This makes it less convenient to use the transmissibility field to denote the presence of this thin low-permeable layer. Therefore, grids with odd number of cells are not considered for later simulations.

We denote by T_h , the ambient transmissibility corresponding to the transmissibility computed between two cells with permeability K_h according to Equations 3.4 and 3.5. We define T_c the transmissibility on the face separating the two sub-reservoirs, at the centre of the grid. This is the parameter we want to alter to simulate a slowdown of the flow. However, we do not directly search for a value of T_c but rather look for the correct multiplier β such that generating flows on coarse grid where $T_c = \beta \times T_h$ will yield good flow approximations. Hence, we want to find an expression of β depending on the physical

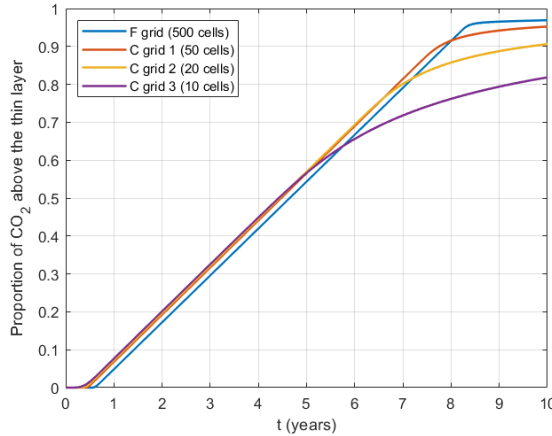


Figure 4.12: Share of the initial CO₂ quantity flowing into the upper reservoir. The face transmissibility at the centre of the reservoir in coarse grids T_c is given by $T_c = 0.042T_h$, with T_h the transmissibility computed for other faces between two cells with identical high permeability.

parameters of the reservoir.

$$\beta = \beta(K_l, e_l, e_h). \quad (4.11)$$

Note that β has not been described as potentially depending on K_h . This corresponds to the fact that, although T_c may depend on K_h , this dependence is handled by T_h .

4.3.2 Results

Search for an initial value of T_c

Searching for the appropriate low transmissibility value, has been done through the same iterative process than the one described in Section 4.2.2 when searching for the lower permeability value K_{lc} .

It was found that the best approximations were obtained when we considered $\beta = 0.042$, independently of n_c . Hence the transmissibility at the frontier between the upper and lower reservoir in coarse grid was multiplied by a coefficient equal to $\beta = 0.042$. Figure 4.12 compiles the evolution of the quantity of CO₂ flowing in the upper reservoir for the fine grid and the coarse grids whose transmissibility field had been altered as described above. Once again, the resemblance between the curves during the ramp-up is striking-out and although an offset appears, the rate of CO₂ permeating into the upper reservoir is identical during several years to the one obtained in the fine grid. The presence of an offset can be explained by the fact that there is no proper layer holding or slowing down the flow of CO₂. Hence, the flow reaches the centre of the reservoir much faster and, despite the altered flow through the interface, it permeates earlier in the upper reservoir.

We also notice that altering the transmissibility field rather than the permeability field does not provide any significant advantages when it comes to the end-phase of CO₂ upward

migration. The remaining quantities of CO₂ trapped in the lower reservoir after the ramp-up phase leak much more slowly in the upper reservoir in coarse grid simulations.

Still, this was considered as a satisfying approximation since the flow rate of CO₂ is well estimated, at least during the ramp-up phase. The difference between the proportion obtained on the fine grid and a coarse grid is constant during the ramp-up phase which means that the rate difference is 0.

Low permeability K_l

The influence of the low permeability value K_l in the initial physical problem was the first parameter investigated. In hindsight to the findings of Section 4.2.2, we could expect the multiplier to be proportional to K_l . In order to verify whether this assumption hold or not, we defined fine grids where the low permeability value was modified. For each of these fine grids, associated coarse grids were defined and had their transmissibility field adjusted according to Equation (4.11) and to the proportionality hypothesis.

Figure 4.13 regroups 4 graphs depicting the flow of CO₂ from the lower reservoir to the upper reservoir for 4 different low permeability values K_l . The first impression left by these 4 graphs is that the altered transmissibility as given in Equation (4.11) is fairly consistent under changes in values of K_l .

On a closer inspection however, it seems that CO₂ flows a bit too fast when the low permeability K_l was set inferior to $0.1K_h$ (Figures 4.13a and 4.13b) and a bit too slow in the opposite case (Figures 4.13c and 4.13d). This can be further confirmed by looking at the error term.

This means that the hypothesis postulated earlier about the proportionality between K_l and β is unfounded and although β does depend on K_l , the dependence is not linear.

Then, we looked for the accurate version of the multipliers depending on the lower permeability value. In Figure 4.14, the simulations displayed have been run using the corrected value for the multiplier depending on the fine grid's lower permeability. By corrected value we mean that the multiplier corresponds to the value generating a flow on the coarse grid that is the best approximation possible of the fine grid flow.

We performed a linear regression on the values of β as a function of K_l and obtained that

$$\beta = K_l^{n_l} \times H(e_l, e_h), \quad (4.12)$$

with $n_l \approx 1.05$. Although this unusual dependence on K_l was derived and already hints at limits of this method, we pursued our work to get a good overview of the dependence of β on other physical parameters.

Thickness of the low-permeable layer e_l

In the previous section, the impact of the low-permeable layer's thickness on the CO₂ flow and the subsequent choice for the appropriate permeability field for a coarse grid were investigated. A similar investigation is conducted to determine how this thickness impacted CO₂ flow approximations on coarse grids with altered transmissibility fields.

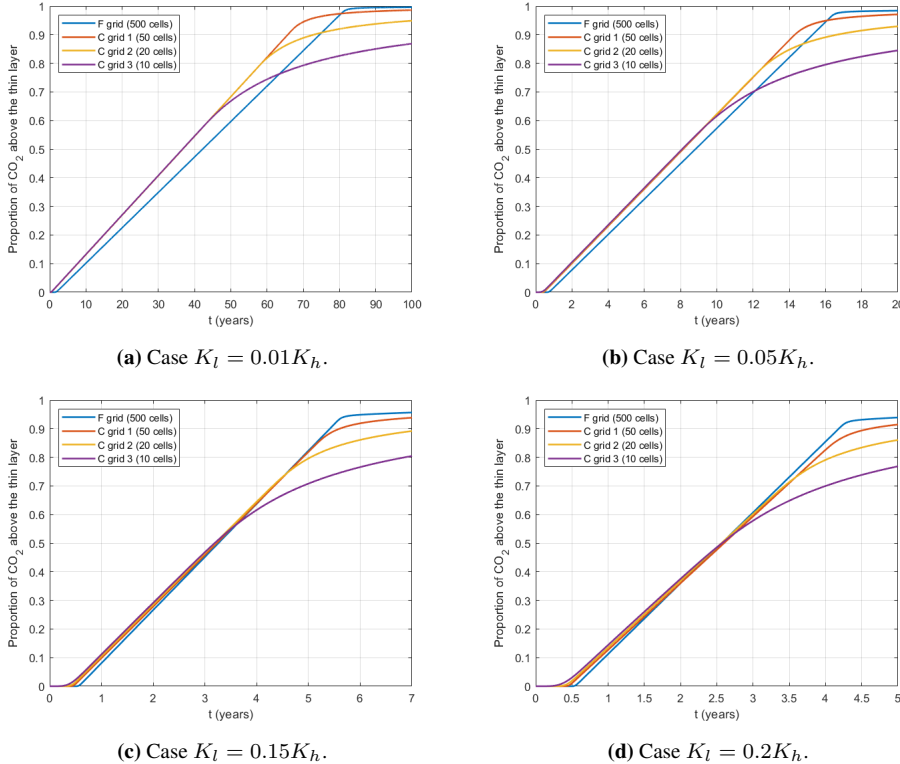


Figure 4.13: Comparison of the evolution of quantities of CO_2 flowing in the upper reservoir on fine grids and some of their associated coarse grids. The multiplier altering the transmissibility T_c is assumed to be proportional to K_l : $T_c = 0.42 \times K_l T_h$.

Simulations where the low-permeable layer's thickness was changed were run and two illustrative examples of such simulations are given in Figure 4.15. The computed evolution of the quantity of CO_2 in the upper reservoir when the thickness of the low-permeable layer in the fine grid are respectively $e_l = 0.6 \text{ m}$ and $e_l = 2 \text{ m}$ are displayed in Figures 4.15a and 4.15b. In hindsight to the findings from the previous method, the thickness of the low-permeable layer had been assumed to have no impact on the low transmissibility value. Therefore, the multiplier used for these simulations was the same and curves obtained on the coarse grids with the same number of cells are identical in these two graphs and in Figure 4.12.

When comparing these two graphs and the graph obtained initially in Figure 4.12, we see that changes in the thickness of the low-permeable layer impact the time at which the ramp-up phase starts but do not affect the rate of CO_2 flowing in the upper reservoir during this ramp-up phase. In these simulations, flow rates computed on the coarse grids approximate rather well the one generated on the fine grids.

Because of this induced offset, the coarse grid curves fit best the curve obtained on the fine

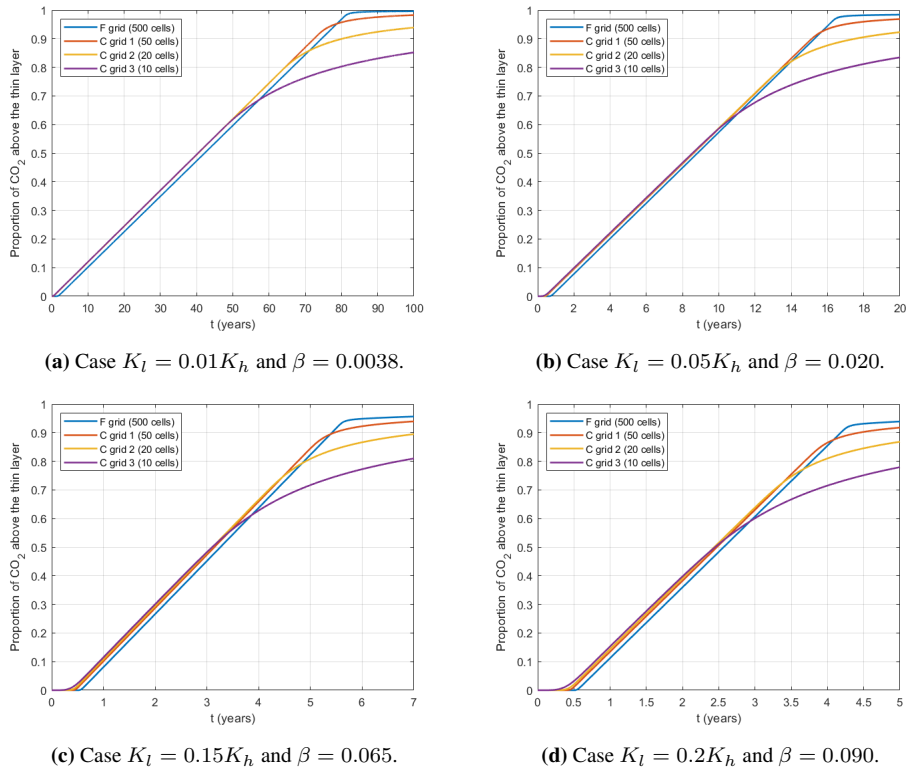


Figure 4.14: Comparison of the evolution of quantities of CO_2 flowing in the upper reservoir on fine grid and some of their associated coarse grids. This time, the multiplier is no longer considered as proportional to K_l and was determined by supplementary simulations. The transmissibility at the centre interface is given by $T_c = \beta T_h$.

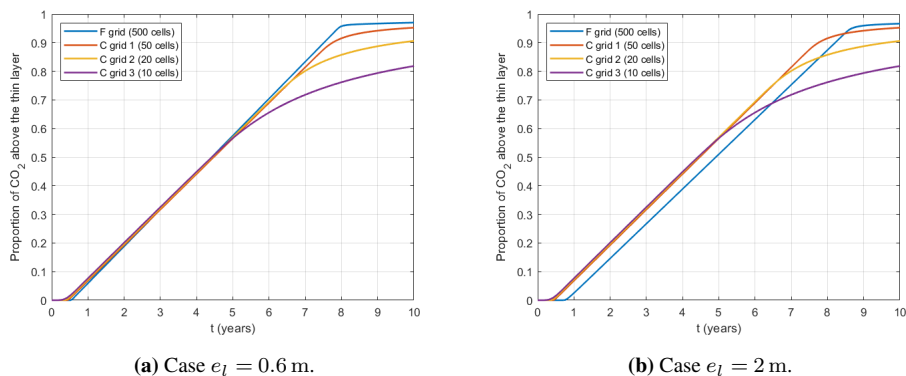


Figure 4.15: Comparison of the evolution of quantities of CO_2 flowing in the upper reservoir on a fine grid and three coarse grids when the thickness of the thin low-permeable layer varies.

grid when the low-permeable layer is small: an increase in the thickness will increase the offset and delay the arrival of CO₂ in the upper compartment. This highlights a limit of this method where the fine grid rate can be approached but it is not possible to denote that CO₂ may spend more time being "stuck" in the low-permeable layer before emerging and permeating into the upper reservoir if the layer is too thick.

Therefore, the low-permeable layer's thickness does not impact the choice of the multiplier on coarse grids and we can rewrite Equation (4.11) as

$$\beta = \beta_0 \times K_l^{n_l}. \quad (4.13)$$

Influence of the initial state

Similarly to what had been done in Section 4.2, the effect of the initial state on the quality of the approximation had been neglected at first to focus on the impacts of the geophysical parameters of the rock.

Given that the initial state has been proven to affect the flow approximation in the preceding method, it was also investigated for the current transmissibility method.

In hindsight to the previous findings, we directly addressed the problem as dependent on the quantity of CO₂ in the reservoir rather than on the precise initial distribution of fluid.

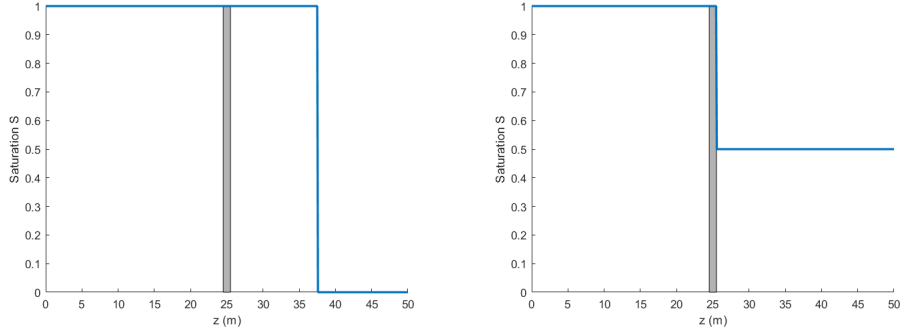
In Figure 4.16, two simulations have been run for an identical quantity of CO₂, half of the lower reservoir filled, and different initial distribution. The initial saturation profiles are given in Figures 4.16a and 4.16b and their associated respective flow of CO₂ through the low-permeable layer are given in Figures 4.16c and 4.16d.

Comparing the evolution of the CO₂ permeating into the upper reservoir in these two cases shows that both initial states let relatively untouched the quality of the approximation of the flow generated by the transmissibility field on the coarse grids. This result is similar to the conclusion made after analysis of Figure 4.10.

Nevertheless, we also looked at scenarios where there was less CO₂ trapped in the reservoir. For instance, we defined three initial states where the quantity of CO₂ initially present in the lower reservoir corresponded to a quarter of the sub-reservoir's volume and ran the simulations on the fine grid and the coarse grids whose permeability field has been altered according to Equation (4.11).

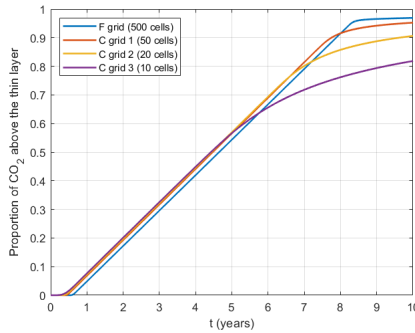
These initial states and the resulting flow of CO₂ through the thin layer are described in Figure 4.17. Then again, we see that the distribution only mildly affects the curves of the CO₂ share in the upper reservoir for a given number of cells in the coarse grid.

However, and as already noticed in Figure 4.11, the fine grid flow approximation gets worse and worse as the coarse grid resolution decreases. For the coarse grid with 20 cells, although the flow rate is somewhat well approximated for a few years, the flow rate obtained on the coarse grid deviates from the fine grid's flow rate much earlier and an offset during the ramp-up phase also denotes that the quality of the approximation is decreased. For the 10-cell coarse grid, it does not even seem that the flow of CO₂ across the thin layer has a *ramp* phase where the inflow of CO₂ is constant on a given time frame, thus denoting

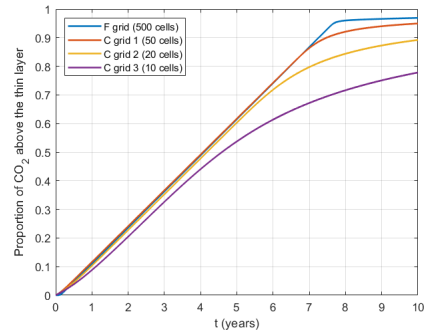


(a) Initial state corresponding to the scenario 1, which has been used for simulations in this section so far.

(b) Initial state where the whole lower reservoir is partially filled with CO_2 .



(c) Share of CO_2 as obtained for the initial state given above, known as scenario 1.



(d) Share of CO_2 as obtained for the initial state given above.

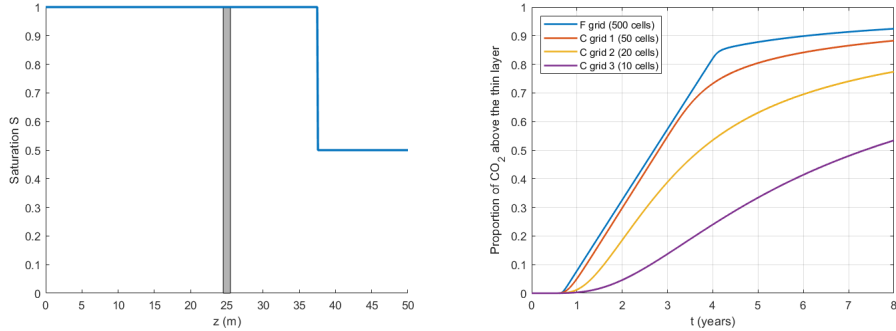
Figure 4.16: Saturation profiles at initial time and their associated graphs depicting the leakage of CO_2 into the upper compartment for a fine grid and three associated coarse grids with altered transmissibility field. The two initial states were defined to fill half of the lower reservoir with CO_2 but with a different distribution within the compartment.

that the current transmissibility at the centre is unable to generate the good flow exchanges between the two compartments.

4.3.3 Overview and discussion

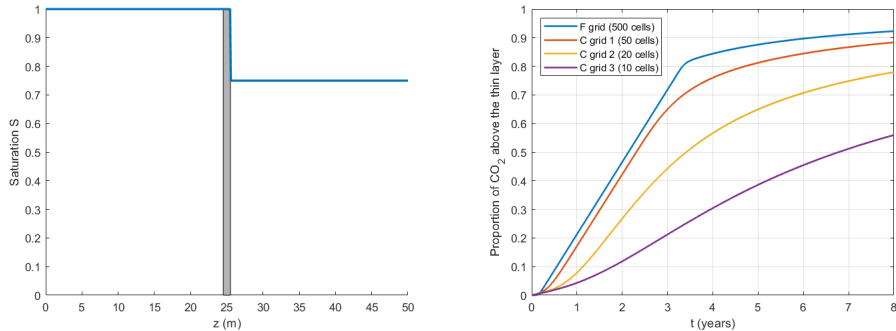
In many ways, altering the transmissibility field yields results similar to the ones obtained by altering the permeability field on coarse grids. In most cases, it is possible to derive or determine a transmissibility at the middle of the reservoir which slows down the flow and generates a flow between the lower and upper reservoir which is similar to the flow obtained for the fine grid (at least during a ramp-up phase).

It was possible to reduce the number of parameters that could influence the choice for T_c or equivalently for the multiplier β . We ended up proving that β depends solely on the lower permeability K_l and that this dependence is *almost* a linear dependence. However,



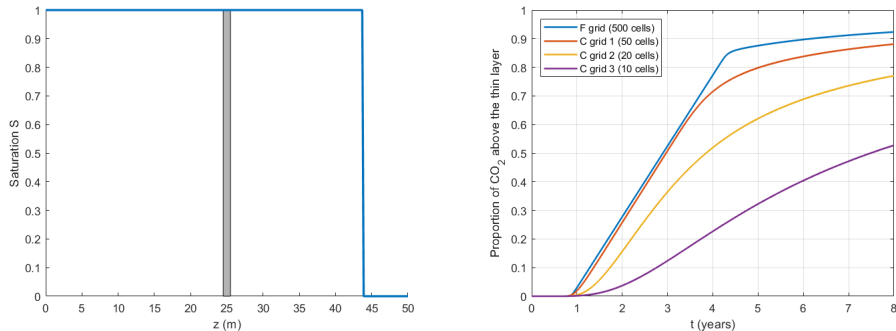
(a) Initial state with CO₂ evenly distributed in the lower part of the lower reservoir.

(b) Flow of CO₂ across the thin layer as generated from the initial state on the left.



(c) Plume of CO₂ homogeneously distributed among the lower reservoir.

(d) Flow of CO₂ across the thin layer as generated from the initial state on the left.



(e) Plume of CO₂ completely stacked at the bottom of the lower reservoir.

(f) Flow of CO₂ across the thin layer as generated from the initial state on the left.

Figure 4.17: Initial states, with different fluid distribution but identical quantity of fluid described (a quarter of the lower compartment is filled with CO₂), and associated flow of CO₂ leaking into the upper compartment for a fine grid and three associated coarse grids with altered transmissibility field.

almost linear is different from being linear. Although it seems convenient to have found an explicit relationship between the lower permeability K_l and β , obtaining such a weird exponent ($n_l \approx 1.05$) really questions the validity of the method. In other words, this strange exponent may actually denote a dependence of T_c on some other parameters that have not been included here (e.g., saturation at the frontier between the sub-reservoirs).

It was also pointed out that the method was inconsistent for changes in the initial state and in particular to the quantity of CO₂ trapped in the reservoir. This further illustrates that this attempt to upscale the transmissibility as a function of the rock parameters only is not sufficient to model the complexity of the studied system and has overlooked other parameters and/or phenomenon that have an impact of the upward migration of CO₂.

Overall, the use of a multiplier to decrease the transmissibility at the centre of the reservoir seems to have the same limitations than the second method had. It is possible to find values of T_c which induce a good approximation of the desired flow rate of CO₂ under given circumstances. However, and as already highlighted, the derived functional relationship cannot be expected to generate good approximations of the fine grid flow behaviour on coarser grids in the general case.

Chapter 5

Conclusion

5.1 Summary and conclusion

Along this thesis, three upscaling methods preserving the effects of thin low-permeable layers of rock on flow behaviour have been implemented, experimented on and discussed.

The first and introductory method considered consisted of harmonic averaging the permeability from the fine grid onto coarser grids. We saw that this method was creating permeability fields on coarse grids that generated flow that were radically different from the fine grid flow. To be more specific, we observed that CO₂ was migrating upward faster than it should have, or in other words, that the lower permeability value computed by the harmonic average let larger quantities of CO₂ permeate through the thin layer.

As a result, we looked for an alternative way to modify the permeability field so that it would lead to simulations where the coarse grid flow would be similar to the fine grid flow. The permeability field was initially described as a function of rock and reservoir parameters only. The various parameters were studied successively to determine their influence on the appropriate choice of the permeability field on coarse grids, and consequently their influence on the choice of the functional relationship between the coarse grid permeability field and the parameters it was assumed to depend on. Along the investigation, it has been shown that it is possible to generate flow on coarse grid that approximates the fine grid flow across the "thin" low-permeable layer. We ended up observing that the lower permeability in the coarse grids was proportional to the lower permeability in the fine grid and that other parameters did not influence the choice of the appropriate permeability field nor did they influence to a large extent the quality of the flow rate approximation. However, it was also determined at the end of the investigation that the initial state can provide plenty of examples where the approximation of the flow was of poor quality or not approximated at all. This highlighted the fact that the assumption made about the functional relationship depending only on physical parameters was too strong and that additional phenomena

depending on the saturation were not taken into account.

The last method that was studied consisted of altering the transmissibility field where the transmissibility is a numerical quantity derived from the TPFA method. We postulated that the thin low-permeable layer could be reduced to a simple alteration of the transmissibility field at the centre of the reservoir for grids with an even number of cells. Moreover, we hypothesised that this new transmissibility at the centre of the column could be described as a function of physical parameters only. Several examples displayed during the investigation illustrate that one can compute transmissibility values on a coarse grid generating great approximations of the fine grid flow. However, for reasons very similar to the ones listed for the previous method, namely that for an identical rock column, and hence an identical transmissibility value at the centre of the rock according to our assumption, various initial saturation profiles can give plenty of distinct flow behaviours. Some may produce flow rate across the interface that is identical to the fine grid flow rate while others may result in very poor approximations of this flow rate. This puts additional emphasis on the fact that intricate phenomena have been neglected and although they may not systematically impact the approximation of the fine grid flow (we did get some encouraging results at times) they may induce errors in the estimation of the flow rate between the two sub-reservoirs.

The key finding to keep in mind is that defining the permeability field or the transmissibility field on a coarse grid as a function of physical parameters of the reservoir and the rock only is generally insufficient to get a complete grasp of all the phenomena that can happen in a two-phase flow evolution.

5.2 Further work

Following the preliminary results derived in this thesis, a natural prolongation would be to properly extend these results to flow barriers (e.g., shale layers) whose permeabilities are considerably lower than the lower permeability value considered along this thesis, $K_l = 0.1$ d. It could be interesting to see how consistent the last two methods presented here hold against layers with very low permeability, for example if K_l was taken in the range of 1 md or less. This needs to be further investigated.

Alternatively, one can also consider studying the solution of a Riemann problem with two discontinuities in the flux function and more specifically determining the limit of the solution as the region between the discontinuities in the flux function shrinks. The latter situation can be compared to the problem studied here and developing Riemann solutions for this problem may yield better results than the methods developed along this thesis as it would probably take into account the saturation dependence that has been overlooked in our functional relationships.

Bibliography

- Darcy, H., 1856. Les Fontaines publiques de la ville de Dijon. V. Dalmont, Paris.
- Eiken, O., Ringrose, P., Hermanrud, C., Nazarian, B., Torp, T.A., Høier, L., 2011. Lessons learned from 14 years of CCS operations: Sleipner, In Salah and Snøhvit. Energy Procedia 4, 5541 – 5548. doi:10.1016/j.egypro.2011.02.541. 10th International Conference on Greenhouse Gas Control Technologies.
- Energy Institute (Great Britain), 2010. Good Plant Design and Operation for Onshore Carbon Capture Installations and Onshore Pipelines: A Recommended Practice Guidance Document. London: Energy Institute.
- Gimse, T., Risebro, N.H., 1991. Riemann problems with a discontinuous flux function, in: Proceedings of Third International Conference on Hyperbolic Problems, pp. 488–502.
- Gimse, T., Risebro, N.H., 1992. Solution of the cauchy problem for a conservation law with a discontinuous flux function. SIAM Journal on Mathematical Analysis 23, 635–648.
- Holden, H., Risebro, N.H., 2002. Front Tracking for Hyperbolic Conservation Laws. volume 152 of *Applied Mathematical Sciences*,. Springer Berlin Heidelberg, Berlin, Heidelberg.
- IPCC, 2018. Global Warming of 1.5C. An IPCC Special Report on the impacts of global warming of 1.5C above pre-industrial levels and related global greenhouse gas emission pathways, in the context of strengthening the global response to the threat of climate change, sustainable development, and efforts to eradicate poverty.
- Kaasschieter, E.F., 1999. Solving the Buckley-Leverett equation with gravity in a heterogeneous porous medium. Computational Geosciences 3, 23–48. doi:10.1023/A:1011574824970.
- Keith, D.W., Dowlatabadi, H., 1992. A serious look at geoengineering. Eos, Transactions American Geophysical Union 73, 289–293. doi:10.1029/91EO000231.
- Langtangen, H.P., Tveito, A., Winther, R., 1992. Instability of Buckley-Leverett flow in

-
- a heterogeneous medium. *Transport in Porous Media* 9, 165–185. doi:10.1007/BF00611965.
- Lie, K.A., 2019. An Introduction to Reservoir Simulation Using MATLAB/GNU Octave: User Guide for the MATLAB Reservoir Simulation Toolbox (MRST). Cambridge University Press. doi:10.1017/9781108591416.
- U.S. Energy Information Administration, 2020. Short-term energy outlook. Available at <https://www.eia.gov/outlooks/steo/> (2020/05/29).
- Welge, H.J., 1952. A simplified method for computing oil recovery by gas or water drive. *Journal of Petroleum Technology* 4, 91–98. doi:10.2118/124-G. sPE.

